Bio-Design and Manufacturing (2025) 8:776–799
https://doi.org/10.1631/bdm.2500021

RESEARCH ARTICLE

Nuclear-targeted reactive oxygen species burst: a self-amplifying nanoplatform that overcomes hypoxia and redox barriers for enhanced sonodynamic cancer therapy

Xiaoyuan Wang[1] · Meng Li[1,2] · Rong Cheng[1,3] · Liting Zhao[4] · Yanfeng Xi[5] · Jianming Wang[6] · Peng Gao[7] · Lingqian Chang[8] · Zixian Liu[1] · Di Huang[9] · Shengbo Sang[1]

Received: 13 January 2025 / Accepted: 8 May 2025

Abstract

Although sonodynamic therapy (SDT) is a promising cancer treatment that induces DNA and macromolecular damage through the generation of reactive oxygen species (ROS), its therapeutic efficacy is limited by local hypoxia and ROS defense mechanisms in tumors. This study proposed a novel tumor treatment approach, focusing on ROS-mediated therapy by targeting the nucleus and depleting glutathione (GSH) levels, which was achieved through a nanoplatform (Pt^{2+}-CDs@PpIX) with integrated functions including GSH detection and depletion, pH-responsive drug release, and nuclear targeting. The Pt^{2+}-CDs@PpIX nanoplatform effectively differentiated normal and cancer cells and also exhibited excellent biocompatibility. Depletion of GSH levels and increased ROS sensitivity of cells significantly improved the effectiveness of SDT, as demonstrated in vitro using Pt^{2+}-CDs@PpIX, which also exhibited significant cellular uptake. Pt^{2+}-CDs@PpIX exerted potent antitumor effects in both two-dimensional and three-dimensional tumor microenvironment models (3DM-7721). Moreover, in 3DM-7721 models, hepatoma cells (SMMC-7721) demonstrated significant inhibition of motility, invasion, and colony formation after exposure to Pt^{2+}-CDs@PpIX. Furthermore, intravenous administration of the Pt^{2+}-CDs@PpIX nanoplatform enabled precise and rapid tumor-targeting, followed by ultrasound-triggered therapy, without adverse effects in nude mice. Hence, this nanoplatform provides a promising strategy for designing cancer therapies and delivering nuclear-targeted drugs.

✉ Zixian Liu
shxy-6868@163.com

✉ Di Huang
huangjw2067@163.com

✉ Shengbo Sang
sunboa-sang@tyut.edu.cn

1 Shanxi Key Laboratory of Artificial Intelligence & Micro Nano Sensors, College of Integrated Circuits, Taiyuan University of Technology, Taiyuan 030024, China

2 Shanxi–Zheda Institute of Advanced Materials and Chemical Engineering, Taiyuan 030024, China

3 Shanxi Institute of 6D Artificial Intelligence Biomedical Science, Taiyuan 030031, China

4 Shanxi Key Laboratory of Otorhinolaryngology Head and Neck Cancer, First Hospital of Shanxi Medical University, Taiyuan 030001, China

5 Department of Pathology, Shanxi Hospital of Cancer Hospital of Chinese Academy of Medical Sciences, Taiyuan 030024, China

6 General Hospital of TISCO, Taiyuan 030809, China

7 BGI, Shenzhen 518083, China

8 Key Laboratory of Biomechanics and Mechanobiology (Ministry of Education), Beijing Advanced Innovation Center for Biomedical Engineering, School of Biological Science and Medical Engineering, Beihang University, Beijing 100191, China

9 Research Center for Nano-Biomaterials & Regenerative Medicine, Department of Biomedical Engineering, College of Artificial Intelligence, Taiyuan University of Technology, Taiyuan 030024, China

Graphical abstract

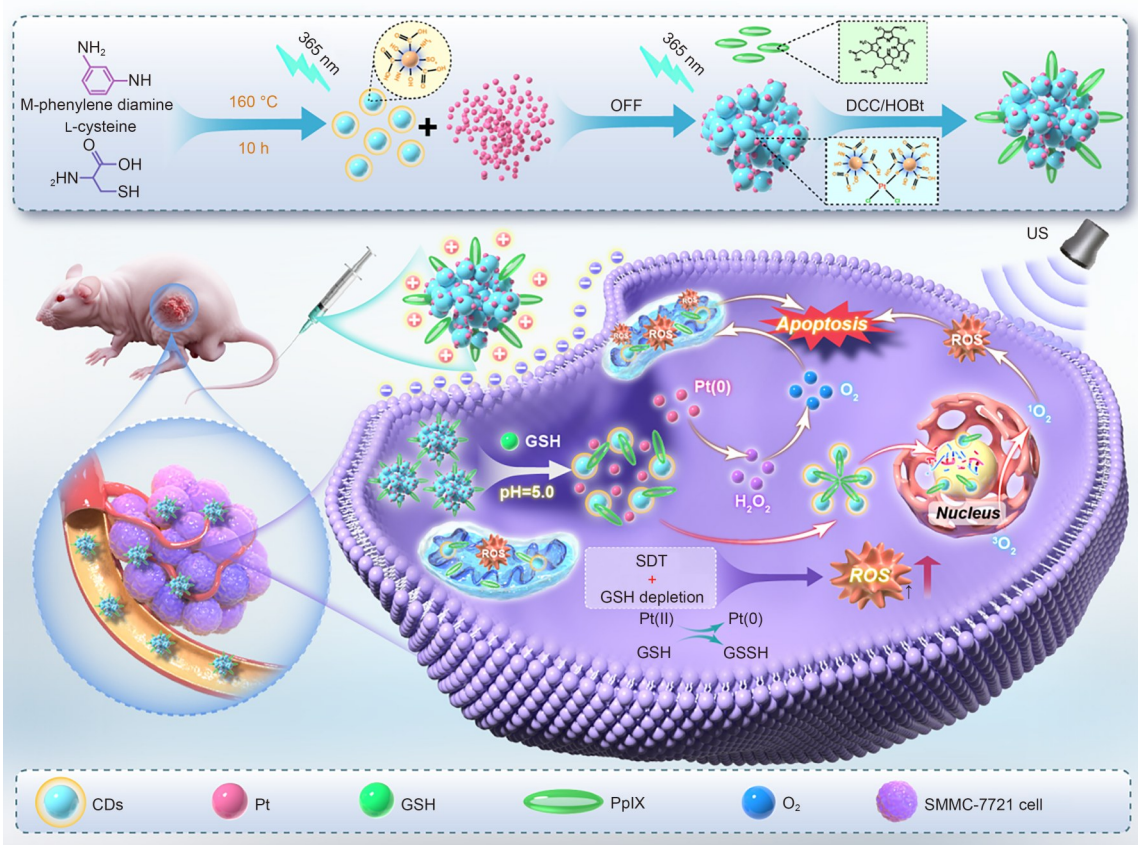

Keywords Sonodynamic therapy · Nuclear targets · Reactive oxygen species · Nanoplatform

1 Introduction

Sonodynamic therapy (SDT) has emerged as a promising alternative to conventional photodynamic therapy (PDT) and chemical dynamic therapy (CDT), providing unique advantages in deep-seated tumor treatment. Unlike PDT that depends on visible/near-infrared (NIR) light with limited tissue penetration (<1 cm) or CDT that requires endogenous metal ions with insufficient reaction kinetics, SDT utilizes low-intensity ultrasound (US) waves capable of penetrating to a depth of >10 cm to activate sonosensitizers, thereby enabling noninvasive therapy for internal tumors [1–3]. This acoustic trigger generates substantial amounts of highly toxic reactive oxygen species (ROS) from oxygen molecules, inducing programmed cell death through oxidative damage to biological macromolecules, particularly DNA [4, 5]. Nevertheless, the overall therapeutic effect of SDT is inevitably affected by several critical factors. First, the hypoxic microenvironment caused by uncontrolled tumor cell proliferation severely impairs the efficient conversion of oxygen (O_2) into ROS [6, 7]. Therefore, the vicious cycle formed by local oxygen consumption and disruption in oxygen supply severely limits the efficiency of SDT [8]. Furthermore, L-glutathione (GSH), the most abundant ROS scavenger in cancer cells, consumes a considerable quantity of ROS generated by US-stimulated sonosensitizers, thereby diminishing the defense mechanism against ROS and mitigating SDT-induced DNA damage [9–11]. Moreover, due to its high sensitivity to ROS and its pivotal role in regulating gene expression to control cellular activities, the cell nucleus is deemed an ideal target for SDT [12–15]. Nevertheless, drug molecules face challenges in penetrating the nuclear membrane barrier after cellular internalization via nanocarriers [16, 17], because the nuclear membrane permits only the passive diffusion of materials with a restricted size range (e.g., <39 nm) [17]. Furthermore, there are limitations, including restricted nuclear accumulation, short targeted retention time, and low cell absorption of drug therapy [18], which result in poor treatment outcomes and significant adverse effects of SDT [19, 20]. Negligence of

these factors will result in incomplete tumor ablation and metastasis [21].

Conventional nanocarriers primarily improve the efficacy of ROS-based tumor therapies by targeting a single factor. For instance, some nanocarriers are loaded with H_2O_2 catalysts (e.g., catalase [22], manganese (IV) oxide (MnO_2) [23], and platinum nanoparticles [24]) to promote the decomposition of endogenous H_2O_2 (100 μmol/L to 1 mmol/L) into oxygen within tumor tissues, thereby mitigating the hypoxia-induced limitations of ROS therapy [25]. Moreover, some nanocarriers are loaded with GSH scavengers and chemotherapeutic drugs [26, 27]. These drugs can bind to intracellular GSH through glutathione S-transferase catalysis and are subsequently effluxed from cancer cells, thereby improving the efficacy of ROS therapy [28, 29]. Because neutrally and negatively charged compounds have difficulty in penetrating the nucleus, modified nanoparticles incorporating cationic amino acids, polyethylenimine, Hoechst 33342 dye, and chitosan have been developed to facilitate nuclear-targeted therapy [30, 31]. In cancer therapy, focusing on a single factor is inadequate; thus, combination strategies—such as chemotherapy, immunotherapy, and other modalities—are indispensable for enhancing therapeutic efficacy [32–35]. Therefore, the integration of improving the hypoxic microenvironment of tumors, inhibiting the ROS defense system after oxidative damage, targeting the nucleus to increase sensitivity to ROS, and improving targeted retention time and nuclear accumulation has provided a novel direction for nanotherapeutic platforms.

This study developed a nanoplatform (Pt^{2+}-CDs@PpIX) for cancer diagnosis and therapy, aiming to improve the efficacy of SDT through multiple mechanisms. The platform was constructed by synthesizing nuclear-targeting carbon quantum dots (CDs), which were modified through an oxidation–reduction reaction with Pt^{4+} to form Pt^{2+}-CDs, followed by conjugation with protoporphyrin IX (PpIX) through an amide reaction. This nanoscale drug delivery system integrates nuclear targeting, pH-responsive drug release, GSH detection and depletion, and improved sonodynamic performance, thereby effectively weakening the ROS defense mechanism and amplifying SDT-induced DNA damage (Fig. 1). The successful fabrication of the system was confirmed through various characterization techniques, and vital SDT parameters were optimized. Its therapeutic efficacy was evaluated in both two-dimensional (2D) and three-dimensional (3D) tumor models, along with evaluations of its biological safety and in vivo performance. To summarize, the Pt^{2+}-CDs@PpIX nanoplatform represents a promising strategy for improving SDT-based cancer therapy, providing novel possibilities for biomedical applications.

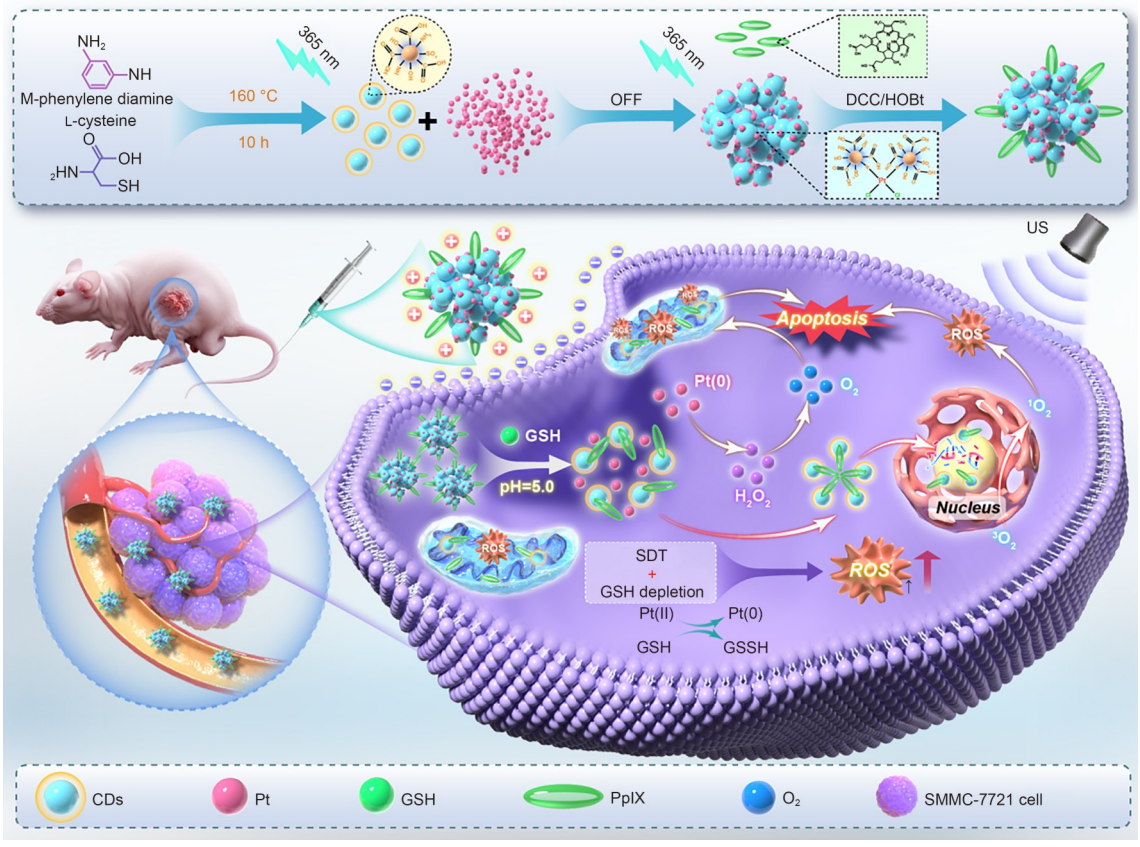

Fig. 1 Schematic of the synthesis and therapeutic application of Pt^{2+}-CDs@PpIX for improved SDT

2 Results and discussion

2.1 Synthesis and characterization of Pt^{2+}-CDs@PpIX

The synthesis process of Pt^{2+}-CDs@PpIX was documented under both natural sunlight and ultraviolet (UV) illumination, as depicted in Fig. 2a. The resulting nanomaterials were further characterized to evaluate their morphology and size distribution. The transmission electron microscopy (TEM) diagram revealed that the CDs, Pt^{2+}-CDs, and Pt^{2+}-CDs@PpIX were spherical and had good dispersion. Their average particle sizes evaluated using the ImageJ software were (2.12±0.03), (2.96±0.61), and (4.28±0.88) nm, respectively (Fig. 2b), which were lower than the diameter of the nuclear pore complex (9–15 nm) and thus conducive to crossing the nuclear membrane and reaching the nucleolus region [36].

Moreover, the composition of different elements in Pt^{2+}-CDs@PpIX was analyzed by energy-dispersive X-ray spectroscopy (EDS) using an Xplore 30 system (Oxford Instruments, UK), where C, N, O, Pt, and other elements were clearly observed. This further indicates the successful preparation of the composites (Figs. S1 and S2 in the supplementary information).

The zeta potential and hydration radius of the prepared materials were characterized. As shown in Figs. 2c and 2d, the charge changed from negative to positive after loading the CDs with Pt^{2+}. This reversal was attributed to the redox reaction between Pt^{4+} and CDs by the addition of K_2PtCl_6 to the surface of the CDs, which inverted the charge and increased the hydration radius from 78.8 to

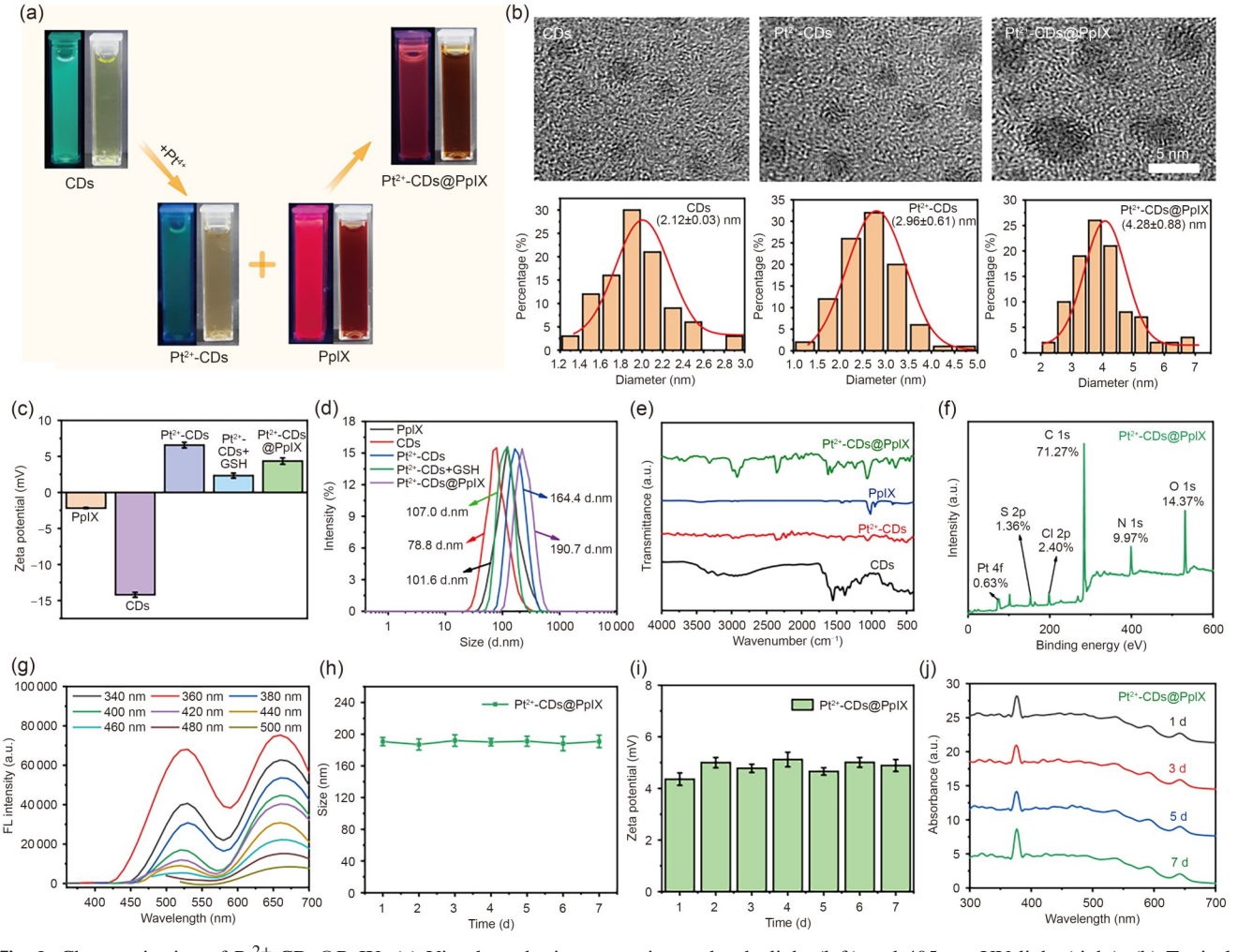

Fig. 2 Characterization of Pt^{2+}-CDs@PpIX. (a) Visual synthesis progression under daylight (left) and 405-nm UV light (right). (b) Typical TEM images and size distributions of CDs, Pt^{2+}-CDs, and Pt^{2+}-CDs@PpIX. Zeta potentials (c), hydrated particle sizes (d), and Fourier transform infrared spectroscopy (FTIR) spectra (e) of CDs, Pt^{2+}-CDs, PpIX, and Pt^{2+}-CDs@PpIX. (f) X-ray photoelectron spectroscopy (XPS) survey of Pt^{2+}-CDs@PpIX (the percentage values in the figure represent the atomic percents). (g) Fluorescence emission spectra of Pt^{2+}-CDs@PpIX under different excitation wavelengths. Stability evaluation of Pt^{2+}-CDs@PpIX in cell culture medium over time, including hydration radius (h), zeta potential (i), and UV–Vis absorbance spectrum (j). Data in (c, h, i) are expressed as mean±standard deviation (n=3)

164.4 d.nm. With the reduction of GSH-induced Pt^{2+} ions, the hydrodynamic size of Pt^{2+}-CDs decreased from 164.4 nm to 107.0 d.nm, and the surface zeta potential decreased from (6.56±2.1) to (2.34±1.6) mV. To address the potential coagulation risks associated with the positively charged surface of nanoparticles (designed to improve nuclear internalization), we systematically investigated their thrombogenic potential using murine anticoagulated whole blood in vitro. As depicted in Fig. S3 (supplementary information), all the tested formulations exhibited blood coagulation indices (BCIs) comparable to the negative control group. Remarkably, there were no statistically significant differences between the experimental group (Pt^{2+}-CDs@PpIX) and controls, confirming that the cationic nanoparticles do not accelerate intrinsic or extrinsic coagulation pathways under physiological conditions. The slightly positive surface charge ((4.36±0.44) mV) of Pt^{2+}-CDs@PpIX serves the following dual purposes: (1) facilitating cellular internalization via electrostatic interactions with negatively charged cancer cell membranes [37] and (2) avoiding the coagulation risks associated with highly cationic nanoparticles [38, 39]. Moreover, to obtain Pt^{2+}-CDs with excellent GSH depletion properties, more Pt ions were required to bind to the CD surface in a redox reaction with the CDs. Therefore, Pt^{2+}-CDs with a size of 78 d.nm were synthesized using K_2PtCl_6 and CDs at a mass ratio of 1:5 (Fig. S4 in the supplementary information).

The composition and surface functional groups of Pt^{2+}-CDs@PpIX were evaluated by Fourier transform infrared spectroscopy (FTIR) and X-ray photoelectron spectroscopy (XPS). In the FTIR spectra (Fig. 2e), the two stretch bands of 3700–3500 and 1690–1630 cm^{-1} in the infrared spectra were amide N–H stretching and amide C=O stretching, respectively, indicating the formation of amide bonds between PpIX and Pt^{2+}-CDs [40, 41]. As depicted in Fig. 2f, Pt^{2+}-CDs@PpIX contains C, O, N, S, Cl, and Pt elements (H elements cannot be detected by XPS), and their atomic percentages are 71.27%, 14.37%, 9.97%, 1.36%, 2.40%, and 0.63%, respectively. The high-resolution spectrum of C1s (Fig. S5a in the supplementary information) has three peaks at 284.1, 285.9, and 288.1 eV, belonging to C–C/C=C, C–N/C–O, and C=O, respectively [42]. In the high-resolution spectra of N 1s, O 1s, S 2p, and Cl 2p (Figs. S5b–S5e in the supplementary information), the peaks at 398.9, 400.1, 531.0, 532.3, 163.2, 164.1, 167.9, 168.3, 169.1, 198.0, and 200.0 eV belong to N–H, C–N–C, C–O, C=O, C–S (S $2p_{3/2}$), C–S (S $2p_{1/2}$), C–SO_2, C–SO_3, C–SO_4, Pt–Cl (Cl $2p_{3/2}$), and Cl^- (Cl $2p_{1/2}$), respectively [40, 43–45]. The high-resolution Pt 4f spectrum of Pt^{2+}-CDs@PpIX exhibits two peaks at binding energies of 72.2 and 75.5 eV (Fig. S5f in the supplementary information), which are assigned to Pt^{2+} ions. The presence of Pt^{2+} ions in Pt^{2+}-CDs was attributed to the reduction of Pt^{4+} by CDs, which has been previously reported to adsorb onto carbon to form Pt^{2+} [3, 46]. These data indicate the presence of abundant surface groups (–COOH, –OH, and –NH_2) in Pt^{2+}-CDs@PpIX, providing Pt^{2+}-CDs@PpIX with good water solubility and excellent fluorescence properties.

The XRD diffraction peaks of Pt^{2+}-CDs@PpIX (Fig. S6 in the supplementary information) include CDs, Pt^{2+}-CDs, and PpIX with sharp diffraction peaks, confirming the successful synthesis of Pt^{2+}-CDs@PpIX. As depicted in Fig. S7 (supplementary information), Pt^{2+}-CDs@PpIX has a new peak between 280 and 320 nm due to the π–π^* transition of the aromatic ring structure in the ultraviolet–visible (UV–Vis) spectra of CDs, Pt^{2+}-CDs, PpIX, and Pt^{2+}-CDs@PpIX [47]. Moreover, four absorption peaks of Pt^{2+}-CDs@PpIX appeared at 500, 540, 577, and 630 nm, which were basically consistent with the UV–Vis spectrum of PpIX, indicating the successful synthesis of Pt^{2+}-CDs@PpIX.

We next examined the optical properties of Pt^{2+}-CDs@PpIX (Fig. 2g). At different excitation wavelengths, there were two peaks at 520 and 660 nm. With an increase in the excitation wavelength, the fluorescence intensity of Pt^{2+}-CDs@PpIX first increased and then decreased, reaching its maximum at 360-nm excitation, and the emission peak position was independent of the excitation wavelength.

The stability of nanomaterials is also a critical factor for investigating their performance for practical applications. Therefore, we systematically examined the colloidal stability of Pt^{2+}-CDs@PpIX in cell culture media over extended periods. As depicted in Figs. 2h–2j, the hydration radius, zeta potential, and UV–Vis absorption spectrum of Pt^{2+}-CDs@PpIX remained virtually unchanged after prolonged incubation in the culture media. These findings demonstrate that the Pt^{2+}-CDs@PpIX nanocomposite maintains excellent colloidal stability under physiological conditions.

2.2 Detection of GSH

Because the surface of Pt^{2+}-CDs is abundant in carboxyl, hydroxyl, amino, and sulfur groups, these functional groups provide them with effective complexation of heavy metal ions. Therefore, as depicted in Figs. S8a and S8b (supplementary information), the fluorescence intensity of CDs is sensitive to the concentration of Pt^{4+}. With an increase in the concentration of Pt^{4+}, the fluorescence intensity of CDs gradually decreases. At a Pt^{4+} concentration of 1.8 μmol/L, the fluorescence intensity of CDs was almost completely quenched. CDs are complexed with metal ions to quench their fluorescence, and the metal ions form complexes with other chelates to restore their fluorescence [48]. In this study, GSH was found to restore the fluorescence of Pt^{2+}-CDs (Fig. 3a), with the fluorescence intensity gradually increasing in a concentration-dependent manner (Fig. 3b).

This effect can be attributed to the ability of GSH to capture Pt^{2+} from the Pt^{2+}-CDs complex, reduce it to metallic platinum [Pt(0)], generate oxidized glutathione (GSSG), and consequently recover the fluorescence of CDs. At a GSH

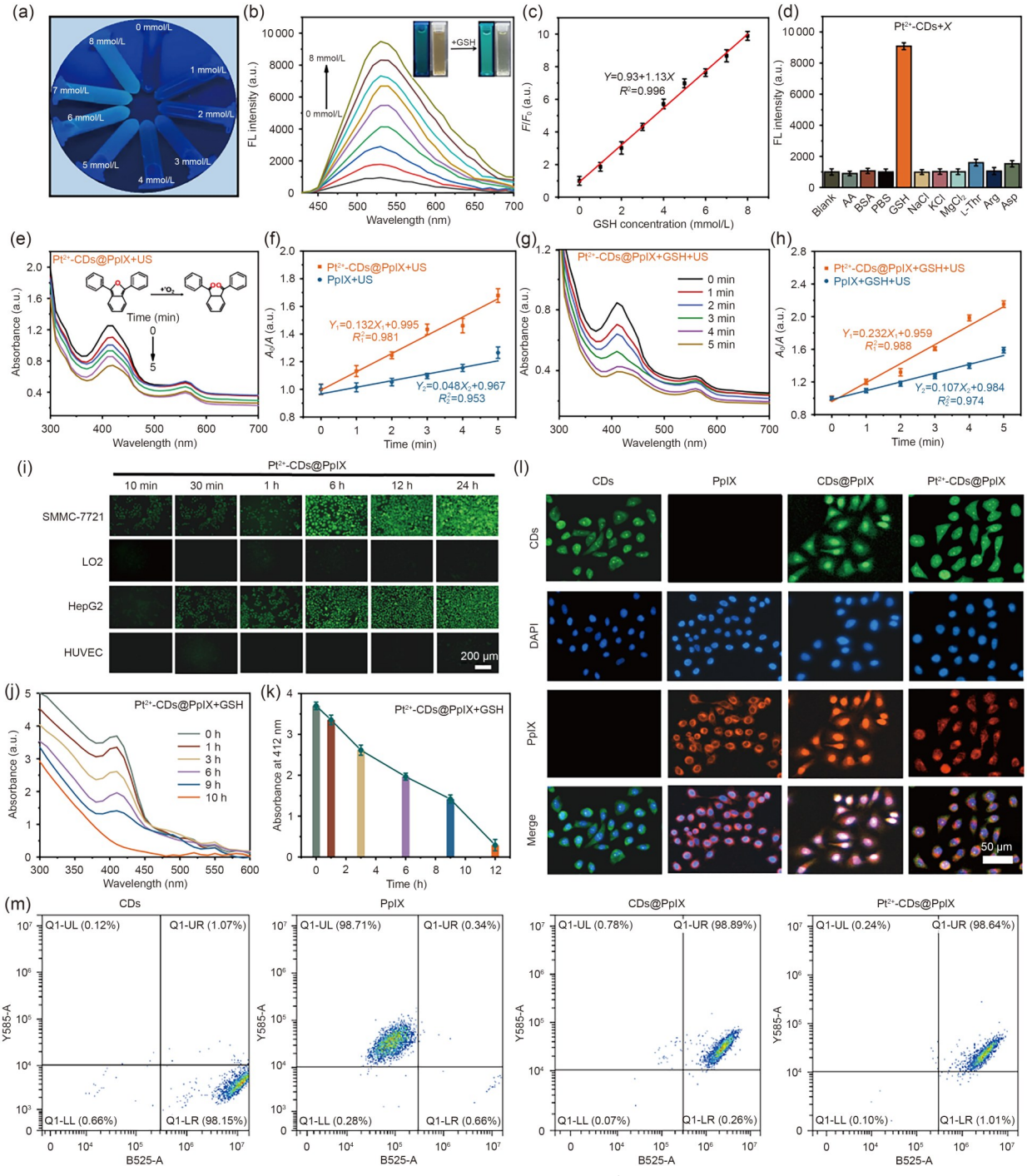

Fig. 3 GSH-responsive fluorescence recovery and $^1O_2$ generation performance of Pt^{2+}-CDs@PpIX. (a) Fluorescence enhancement upon GSH addition. (b) Fluorescence spectra of Pt^{2+}-CDs with increasing GSH concentrations (0–8 mmol/L). (c) Linear relationship of fluorescence intensity (F/F_0) at 530 nm versus GSH concentration. (d) Selectivity of Pt^{2+}-CDs for GSH over other biomolecules. (e–h) Time-dependent $^1O_2$ generation of Pt^{2+}-CDs@PpIX and Pt^{2+}-CDs@PpIX+GSH under US, with kinetic analyses and comparisons with free PpIX. (i) Fluorescence images of different cell lines (SMMC-7721, LO2, HepG2, and HUVEC) incubated with Pt^{2+}-CDs@PpIX over time. (j, k) GSH depletion ability of Pt^{2+}-CDs@PpIX using the DTNB assay. (l) Intracellular uptake of free CDs, PpIX, CDs@PpIX, and Pt^{2+}-CDs@PpIX in SMMC-7721 cells assessed by fluorescence microscopy. (m) Flow cytometry analysis of intracellular uptake efficiency in SMMC-7721 cells. Data in (c, d, f, h, k) are expressed as mean±standard deviation (n=3). LO2: human normal hepatic cell line; HepG2: human hepatocellular carcinoma cell line; HUVEC: human umbilical vein endothelial cell; DTNB: 5′-dithiobis-(2-nitrobenzoic acid)

concentration of 8 mmol/L, the fluorescence intensity of CDs was completely restored. Therefore, Pt^{2+}-CDs can be used to detect GSH. Within the concentration range of 0–8 mmol/L, a strong linear correlation was detected between GSH concentration and Pt^{2+}-CDs fluorescence intensity. The linear regression equation can be expressed by the following formula: Y=0.93+1.13X, and the correlation coefficient was R^2=0.996 (Fig. 3c). The detection limit of this method was calculated as 1.8 μmol/L using the formula LOD=3S_D/k, where S_D is the standard deviation of the blank signal and k is the slope of the calibration curve. The quenched Pt^{2+}-CDs could selectively detect GSH (Fig. 3d). Therefore, Pt^{2+}-CDs can detect GSH with high sensitivity and selectivity and also have a wide detection range (0–8 mmol/L) and low detection limit (1.8 μmol/L).

We then measured the efficiency of $^1O_2$ formation under US irradiation using a 1,3-diphenylisobenzofuran (DPBF) probe to determine the sonodynamic performance of Pt^{2+}-CDs@PpIX in the presence and absence of GSH [8]. In the absence of GSH, the $^1O_2$ generation efficiency was 2.75 times higher than that of the original PpIX (0.048 min^{-1}) under the same US irradiation conditions (Fig. 3e), whereas in the presence of GSH, the singlet oxygen ($^1O_2$) generation efficiency of Pt^{2+}-CDs@PpIX was 0.232 min^{-1} (Fig. 3f). In contrast, the rate constant of $^1O_2$ generation in the Pt^{2+}-CDs@PpIX group was 0.132 min^{-1}, which was significantly lower than that in the Pt^{2+}-CDs@PpIX+GSH group (Figs. 3g and 3h). Moreover, the $^1O_2$ generation efficiency of CDs@PpIX+GSH+US was lower than that of Pt^{2+}-CDs@PpIX+GSH+US (Fig. S9 in the supplementary information), indicating that Pt^{2+}CDs@PpIX can enhance ROS generation upon US activation. These data suggest that Pt^{2+}-CDs@PpIX possesses the ability to overcome GSH-mediated resistance to SDT in cancer cells compared with CDs@PpIX without Pt^{2+}.

2.3 Screening of cells by Pt^{2+}-CDs@PpIX

We explored the potential of Pt^{2+}-CDs as GSH-responsive fluorescent probes for tumor diagnosis by fluorescence imaging, for which we used the human normal hepatic cell line (LO2), the human umbilical vein endothelial cell (HUVEC) line, and the human hepatocellular carcinoma cell line (SMMC-7721, HepG2). In normal tissues, intracellular GSH concentrations range from 2 to 10 mmol/L, whereas extracellular GSH levels are much lower (2–10 μmol/L). In tumor cells, GSH concentrations are 4–7 times higher than those in normal cells [49, 50]. As shown in Fig. S10a (supplementary information), free CDs that were insensitive to GSH act as fluorescence imaging probes, and when incubated with normal and cancer cells, they were immediately internalized into the cytoplasm of all these cells, with no fluorescence contrast distinction between normal and cancer cells. Pt^{2+}-CDs@PpIX and Pt^{2+}-CDs were used as GSH-sensitive fluorescent probes (Fig. 3i; Fig. S10b in the supplementary information). Both Pt^{2+}-CDs@PpIX-labeled and Pt^{2+}-CDs-labeled normal LO2 cells and HUVECs remained "negative" (exhibiting minimal fluorescence contrast) even after 24 h of incubation. In contrast, SMMC-7721 and HepG2 cells exhibited a high fluorescence contrast ("positive") after 6 h of incubation. With an increase in the incubation time, the fluorescence intensity within the hepatoma cells gradually stabilized through a slow clearing of GSH in the cytoplasm. Further analysis by flow cytometry (Fig. S11 in the supplementary information) confirmed the reliability of these results (Fig. 3i). In vitro fluorescence imaging revealed that Pt^{2+}-CDs and Pt^{2+}-CDs@PpIX can be used as GSH-sensitive fluorescent probes, which have significant potential in GSH marker-based tumor diagnosis.

We next investigated the GSH depletion capacity of Pt^{2+}-CDs and Pt^{2+}-CDs@PpIX composites using 5′-dithiobis-(2-nitrobenzoic acid) (DTNB) as the detection index of GSH [8]. As illustrated in Figs. S10c and S10d (Pt^{2+}-CDs in the supplementary information) and Figs. 3j and 3k (Pt^{2+}-CDs@PpIX), the characteristic absorbance peak of DTNB (412 nm) decreases dramatically with increasing incubation time, indicating that Pt^{2+}-CDs and Pt^{2+}-CDs@PpIX deplete GSH levels. No significant difference was observed in GSH consumption between the two samples. Therefore, both materials can be used to determine the detection and consumption of GSH.

2.4 Nuclear targeting performance of Pt^{2+}-CDs@PpIX

The cellular internalization effect of Pt^{2+}-CDs@PpIX was observed by fluorescence microscopy. CDs and PpIX will fluoresce under excitation, which can track the Pt^{2+}-CDs@PpIX system, and the nuclei of SMMC-7721 cells were stained with the commercial dye 4',6-diamidino-2′-phenylindole (DAPI), which can localize the nuclei. Thus, we investigated the cellular uptake and subcellular localization of CDs, PpIX, CDs@PpIX, and Pt^{2+}-CDs@PpIX. As depicted in Fig. 3l, after 1 h of incubation with SMMC-7721 cells, Pt^{2+}-CDs@PpIX was rapidly endocytosed into the cells and released PpIX, which manifested as red fluorescence in the cytoplasm and nucleus, whereas only the cytoplasm of the free PpIX group demonstrated red fluorescence. The reason for this phenomenon was that Pt^{2+}-CDs carried PpIX into the nucleus and achieved nuclear targeting function, and Pt^{2+}-CDs@PpIX showed green fluorescence, whereas free PpIX did not. Furthermore, compared with the results obtained using the commercial dye DAPI, the red fluorescence of Pt^{2+}-CDs@PpIX and the blue fluorescence of DAPI coincided, which further indicates that

Pt^{2+}-CDs@PpIX achieved the function of nuclear targeting. Nevertheless, compared with the red fluorescence of CDs@PpIX, the intensity of Pt^{2+}-CDs@PpIX red fluorescence in the cytoplasm was obviously weaker, which is due to the fact that the Pt^{2+}-CDs@PpIX nanoplatform possesses a slow release capability, and the stability of the system was significantly improved. The results of flow cytometry depicted in Fig. 3m further corroborate these findings, demonstrating a stronger red fluorescence in the CDs@PpIX group than in the Pt^{2+}-CDs@PpIX group. These data indicate a significant increase in the cellular uptake and nuclear transport of CDs@PpIX and Pt^{2+}-CDs@PpIX compared with those of free PpIX.

To obtain the maximum drug-loading rate, we designed Pt^{2+}-CDs and PpIX with different mass ratios for the amide reaction. As illustrated in Fig. S12a (supplementary information), the absorbance response of PpIX was strongest under pH 6.2, which was thus selected for the loading condition. As depicted in Fig. S12b (supplementary information), when the mass ratio was 2:1, the loading rate of PpIX reached the maximum, and its drug-loading rate was 88.4%, which is due to the optimal ratio of amino groups carried by carboxyl and Pt^{2+}-CDs on PpIX under this condition. We further explored the drug release phenomenon of Pt^{2+}-CDs@PpIX. As shown in Fig. S13 (supplementary information), the cumulative release of PpIX in CDs@PpIX and Pt^{2+}-CDs@PpIX systems at pH 5.0 was higher than that at pH 7.4, indicating the pH-responsive characteristics of the two systems. Under acidic conditions, the amide bond between Pt^{2+}-CDs and PpIX hydrolyzes, causing the release of PpIX.

2.5 Antitumor efficacy of Pt^{2+}-CDs@PpIX in vitro

To explore the therapeutic efficacy of Pt^{2+}-CDs@PpIX system-mediated SDT on SMMC-7721 cells, we conducted tests on the intensity and duration of US, with the results depicted in Fig. S14 (supplementary information). We found that the viability of SMMC-7721 cells decreased in a sonication time-dependent manner under sonication at 1.5 W/cm^2 (Fig. S14a in the supplementary information) and also significantly decreased in a US intensity-dependent manner, with significant inhibition at 1.5 W/cm^2 US (Fig. S14b in the supplementary information). To summarize, the greatest inhibitory effect on tumor cells was observed at a US intensity of 1.5 W/cm^2 and a US duration of 10 min.

The cell counting kit-8 (CCK-8) assay was performed to explore the biocompatibility of the Pt^{2+}-CDs@PpIX sonosensitizer, wherein SMMC-7721 cells were incubated to evaluate its superior in vitro SDT performance. Without US irradiation, CDs, PpIX, Pt^{2+}-CDs, CDs@PpIX, and Pt^{2+}-CDs@PpIX agents exhibited no cytotoxicity even at a concentration of 100 μg/mL (Fig. 4a; Fig. S15 in the supplementary information). However, under US irradiation (1.5 W/cm^2) for 10 min, the viability of SMMC-7721 cells incubated with Pt^{2+}-CDs@PpIX decreased rapidly in a concentration-dependent manner (Fig. 4b). Further analyses showed that Pt^{2+}-CDs@PpIX exerted minimal toxicity and side effects on LO2 cells under US irradiation (Fig. S16 in the supplementary information), demonstrating its selective targeting of cancer cells, because the ROS enhancement effect did not appear in normal cells. Specifically, after incubation under the same US conditions, the viabilities of SMMC-7721 cells treated with PpIX, CDs@PpIX, and Pt^{2+}-CDs@PpIX were 66%, 28%, and 10%, respectively, indicating that the depletion of GSH levels and the combination of PpIX with CDs significantly improved the therapeutic effect of SDT (Fig. 4c). The live/dead costaining experiment confirmed the superior SDT performance of Pt^{2+}-CDs@PpIX (Fig. 4d). We also conducted the 2′,7′-dichlorofluorescin diacetate (DCFH-DA) staining assay to evaluate the intracellular generation of ROS induced by Pt^{2+}-CDs@PpIX under US irradiation. We detected no significant ROS fluorescence signal in the control group of SMMC-7721 cells or in groups exposed to US irradiation alone or Pt^{2+}-CDs@PpIX alone (Fig. 4e). In contrast, we detected a bright ROS fluorescence signal in the Pt^{2+}-CDs@PpIX+US group, confirming that the combination of the nanoplatform improved the intracellular generation of ROS. Subsequently, we applied it to a 3DM-7721 model in vitro, as depicted in Fig. 4f, and the live/dead staining further confirmed its significant therapeutic effect in the 3DM-7721 model. Furthermore, the Pt^{2+}-CDs@PpIX+US group exhibited a significantly higher ROS fluorescence signal than the other groups.

To further detect the pharmacodynamic response of Pt^{2+}-CDs@PpIX+US to SMMC-7721 cells, we analyzed the expression of 8-oxoG, 53BP1, and Bcl-2 proteins in the 3DM-7721 model after treatment with the abovementioned seven groups. The results of quantitative reverse transcription polymerase chain reaction (qRT-PCR) revealed a significant difference in the gene expression levels among the seven groups after treatment. The expression results of hepatoma-related genes (alpha-fetoprotein (*AFP*), *CD24*, and *TGF-β*) demonstrated that the related genes of SMMC-7721 cells were significantly inhibited after Pt^{2+}-CDs@PpIX+US treatment (Figs. S17–S21 in the supplementary information; Fig. 4g). We also measured the relative expression of apoptosis-related genes in the treated cells and found significantly increased mRNA expression levels of *53BP1* and *Bcl-2* after Pt^{2+}-CDs@PpIX+US treatment. We further confirmed that Pt^{2+}-CDs@PpIX+US exerted a significant effect after the external SDT (Fig. 4g).

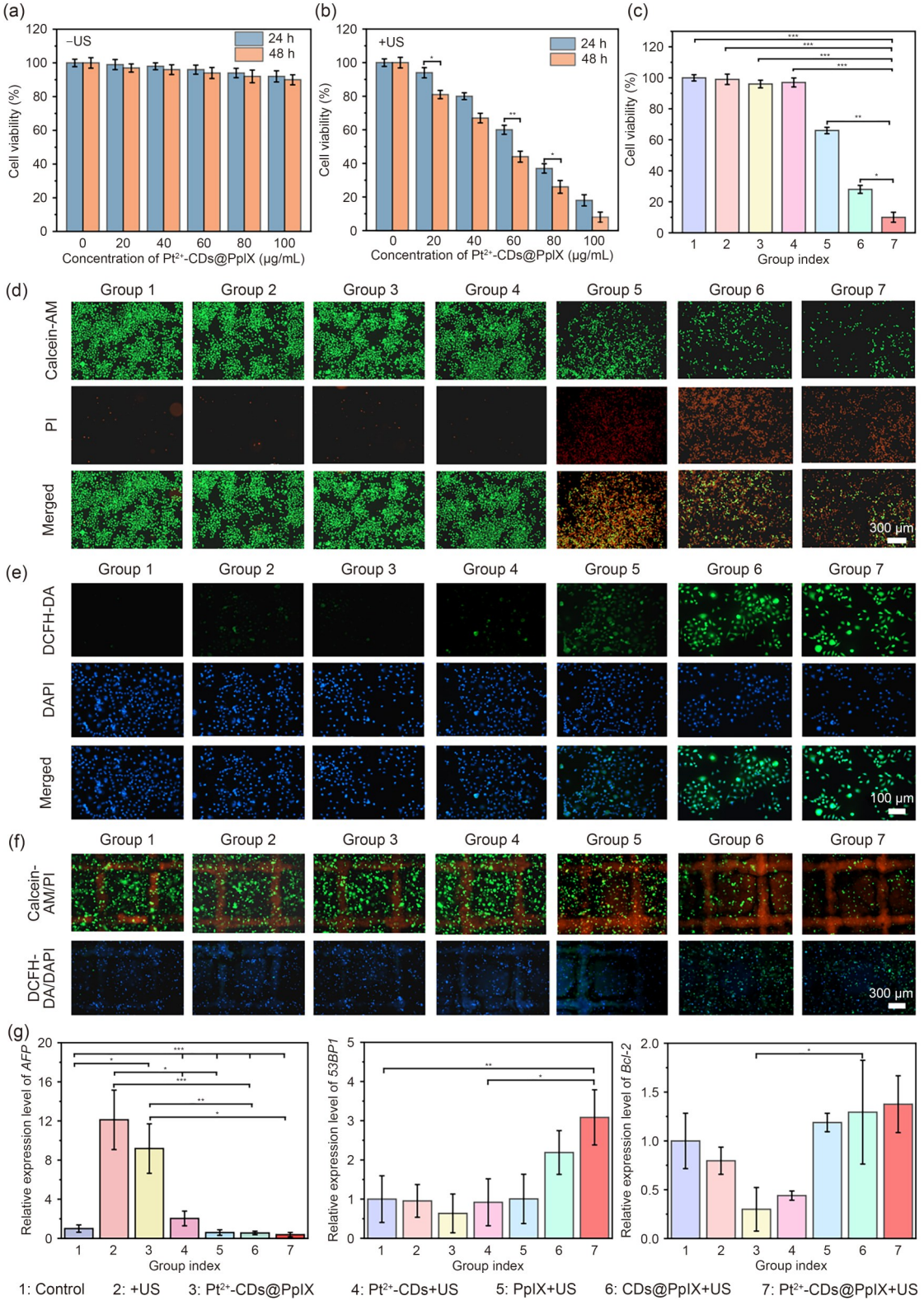

Fig. 4 In vitro evaluation of cytotoxicity, ROS generation, and gene expression in 2D and 3D SMMC-7721 models after treatment with Pt^{2+}-CDs@PpIX and ultrasound. (a, b) Relative viability of SMMC-7721 cells after treatment with different concentrations of Pt^{2+}-CDs@PpIX and Pt^{2+}-CDs@PpIX+US (n=4). (c) Comparison of cell viability among treatment groups (n=4). (d, e) Fluorescence imaging of SMMC-7721 cells in the 2D model stained with PI (propidium iodide)/Calcein-AM (calcein acetoxymethyl ester) for live/dead cell assay and DCFH-DA/DAPI for ROS detection. (f) Corresponding live/dead and ROS imaging in the 3DM-7721 model. (g) qRT-PCR analysis of *AFP* and apoptosis-related gene expression in the 3D model on Day 7 (n=3). $^{*}p<0.05$, $^{**}p<0.01$, $^{***}p<0.001$. Data in (a–c, g) are expressed as mean±standard deviation

2.6 Effects of Pt^{2+}-CDs@PpIX on migration, invasion, and colony formation

The migration, invasion, and antiproliferation ability of Pt^{2+}-CDs@PpIX-treated SMMC-7721 cells in the 3DM-7721 model were evaluated using scratch, Transwell, and colony formation assays. As shown in Figs. 5a and 5b, Pt^{2+}-CDs@PpIX+US-treated SMMC-7721 cells in the 3DM-7721 model exhibited the lowest migration capacity, as determined by the scratch assay. The Transwell assay (Figs. 5c and 5d) further confirmed that SDT combined with Pt^{2+}-CDs@PpIX significantly inhibited cell invasion in the 3DM-7721 model, demonstrating the potent antiproliferative effect of this treatment. Furthermore, SMMC-7721 cells in the 3DM-7721 model cotreated with Pt^{2+}-CDs@PpIX and US irradiation exhibited fewer colonies even at low concentrations (20 μg/mL; Figs. 5e and 5f), suggesting that Pt^{2+}-CDs@PpIX possesses a US-triggered antiproliferative capacity. Overall, these findings demonstrate that Pt^{2+}-CDs@PpIX+US effectively inhibits the proliferation, migration, and invasion of SMMC-7721 cells in the 3DM-7721 model.

To explore the effects of the Pt^{2+}-CDs@PpIX nanoplatform on the proliferation, migration, invasion, and colony formation of SMMC-7721 cells in the 3DM-7721 model, we collected drug-treated SMMC-7721 cells, extracted RNA, and performed cDNA synthesis for qRT-PCR analysis. Results showed significantly downregulated expression levels of the tumor proliferation marker *Ki67* and the stem cell markers *CD133* and *EpCAM*, suggesting reduced invasion, metastasis, drug resistance, and recurrence of SMMC-7721 cells in the 3DM-7721 model after treatment with Pt^{2+}-CDs@PpIX (Figs. 5g–5i) [51–53].

2.7 Treatment mechanism of Pt^{2+}-CDs@PpIX

It is well established that excessive ROS production induced by microenvironmental stimulation can disrupt macromolecular integrity, trigger oxidative stress responses, damage mitochondrial DNA, and ultimately result in apoptosis and necrosis [54]. Moreover, because the nanodrug delivery system can successfully enter the nucleus, it directly damages nuclear DNA, thereby improving the therapeutic efficacy [55, 56]. In this study, immunofluorescence staining

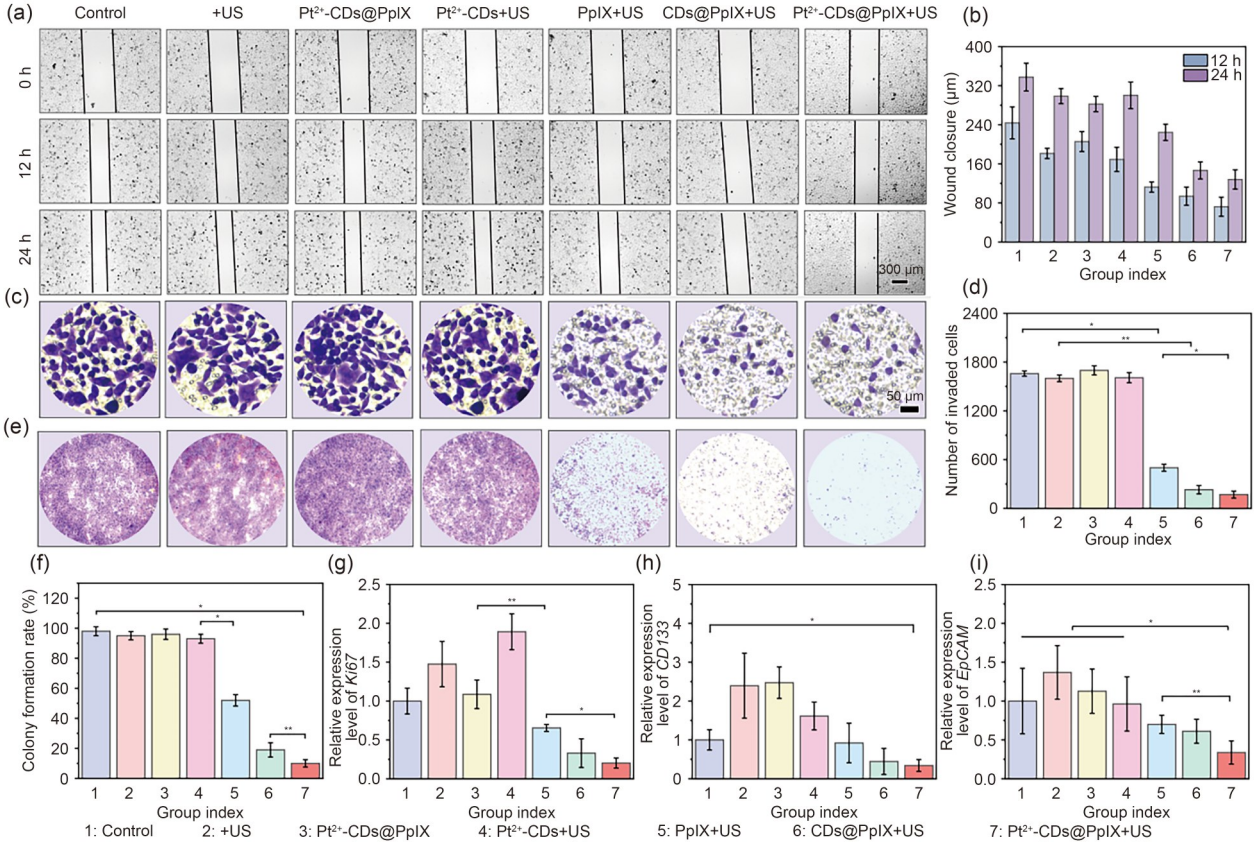

Fig. 5 Evaluation of the migration, invasion, and colony formation of SMMC-7721 cells in a 3D tumor model under different treatments. (a) Wound-healing assay images at 0, 12, and 24 h. (b) Quantification of wound closure shows significantly reduced migration in Group 7 (Pt^{2+}-CDs@PpIX+US). (c, d) Transwell invasion assay and corresponding cell counts indicate the strongest inhibition of invasion in Group 7. (e, f) Colony formation assay images and quantification reveal the lowest colony rate in Group 7. (g–i) mRNA expression levels of metastasis- and proliferation-related markers in treated 3D tumor cells. Data in (b, d, f–i) are expressed as mean±standard deviation (n=3). $^{*}p<0.05$, $^{**}p<0.01$

was performed to detect the expression of 8-oxoG in the different treatment groups. Results showed that Pt^{2+}-CDs@PpIX+US treatment significantly increased the accumulation of 8-oxoG, as indicated by the strong red fluorescence (Figs. 6a and 6b). In the Pt^{2+}-CDs@PpIX nanoplatform, Pt^{2+} depleted the elevated GSH levels within cancer cells. This depletion weakens the antioxidant defense of cells, rendering them more susceptible to oxidative stress. Combined with US-triggered SDT, this increased oxidative stress results in the generation of ROS, which causes DNA damage, as evidenced by the increased 8-oxoG accumulation. Compared with other treatments, the interaction of Pt^{2+}, CDs, PpIX, and US remarkably increased the expression of 8-oxoG, confirming that Pt^{2+}-CDs@PpIX+US induces DNA oxidative damage through ROS production (Figs. 6a and 6b). Another DNA damage-specific marker, 53BP1, was also detected by immunofluorescence. Similar to 8-oxoG staining, an increase in 53BP1 expression in the nuclear region was detected after treatment with Pt^{2+}-CDs@PpIX+US (Figs. 6c and 6d). To summarize, Pt^{2+}-CDs@PpIX+US can induce the massive production of 8-oxoG and 53BP1, which causes extensive damage to the genetic material through base mismatch and ultimately results in programmed apoptosis.

Next, western blotting was performed to evaluate the expression levels of key marker proteins involved in the treatment response. As depicted in Figs. 6e and 6f, Pt^{2+}-CDs@PpIX+US induced DNA damage, triggering p53-mediated apoptosis in cancer cells. p53 expression was upregulated in all treatment groups, with the highest levels observed in the Pt^{2+}-CDs@PpIX+US group (Fig. 6f). Bcl-2 exerts an antiapoptotic effect by preventing cytochrome c

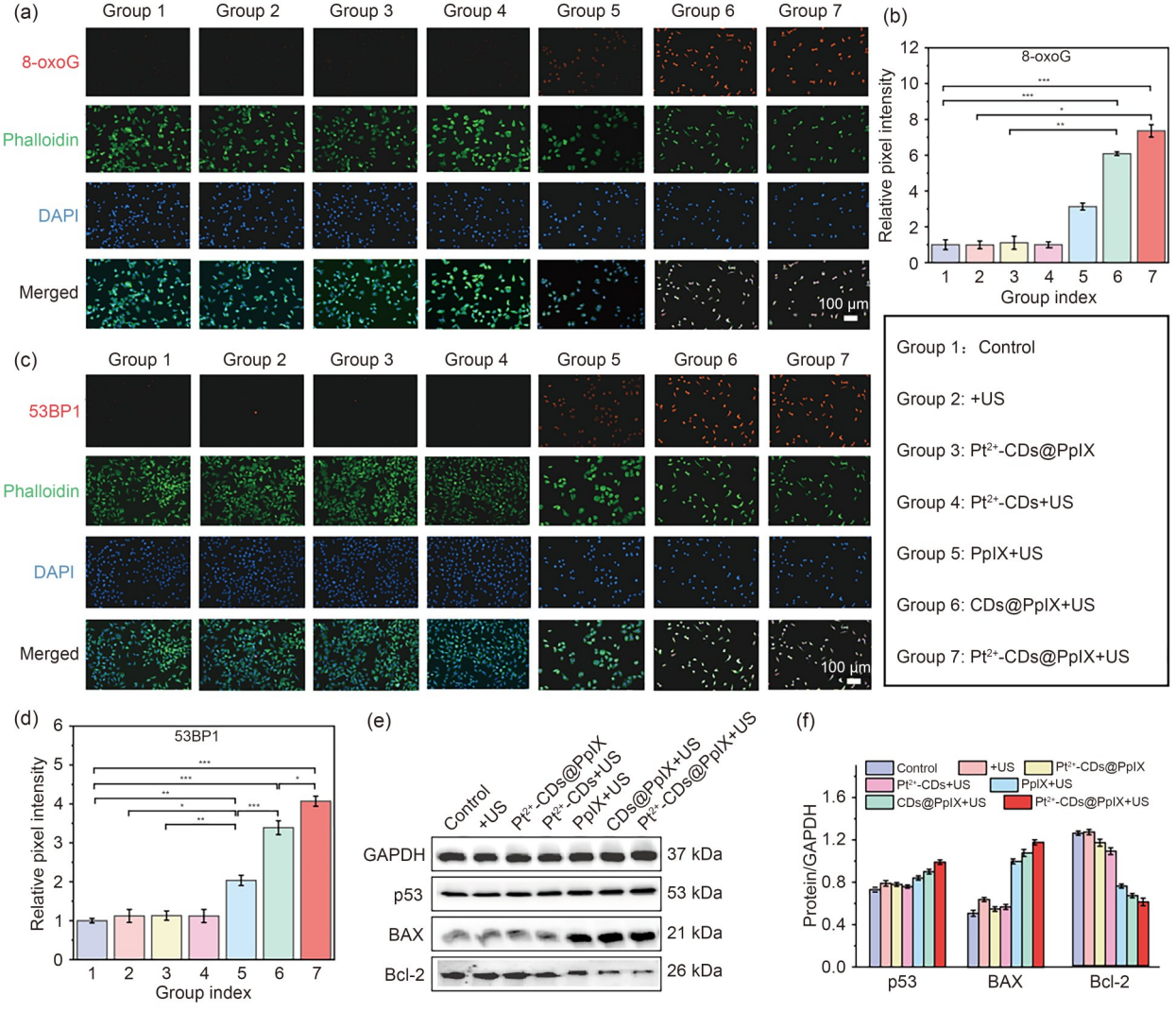

Fig. 6 Mechanistic investigations of DNA damage and apoptosis. (a, c) Immunofluorescence images of 8-oxoG and 53BP1 in SMMC-7721 cells after different treatments. (b, d) Corresponding fluorescence intensity quantification. (e) Western blotting of apoptosis proteins (p53, BAX, and Bcl-2). (f) Quantitative band intensity analysis using ImageJ. Data in (b, d, f) are expressed as mean±standard deviation (n=3). $^{*}p<0.05$, $^{**}p<0.01$, $^{***}p<0.001$

release from mitochondria, whereas BAX promotes apoptosis by increasing mitochondrial outer membrane permeability and facilitating cytochrome c release. As illustrated in Figs. 6e and 6f, BAX and Bcl-2 exhibited contrasting expression trends. The Pt^{2+}-CDs@PpIX+US treatment group exhibited the highest BAX expression and the lowest Bcl-2 expression, confirming that Pt^{2+}-CDs@PpIX+US effectively induced mitochondrial dysfunction, ultimately resulting in the apoptosis of tumor cells.

2.8 Evaluation of the biosafety of Pt^{2+}-CDs@PpIX in vivo

Considering the essential role of biosafety in drug delivery [57, 58], we evaluated the biosafety of the Pt^{2+}-CDs@PpIX nanoplatform in vivo. The results showed that most hematological parameters, including white blood cells (WBCs), mean corpuscular volume (MCV), hemoglobin (HGB), hematocrit (HCT), mean corpuscular hemoglobin (MCH), mean corpuscular hemoglobin concentration (MCHC), red blood cells (RBCs), and platelets (PLT), remained within normal ranges across all groups, with only slight fluctuations at certain time points (Fig. 7a), indicating favorable hematological compatibility. Furthermore, liver and kidney function markers—including aspartate aminotransferase (AST), alanine aminotransferase (ALT), alkaline phosphatase (ALP), and blood urea nitrogen (BUN)—showed no significant abnormalities among the four groups, despite minor fluctuations in AST and ALP levels (Fig. 7a). Moreover, we evaluated the potential damage caused by Pt^{2+}-CDs@PpIX to mouse organs. The results of hematoxylin and eosin (H&E) staining showed that the structures of the heart, liver, spleen, lung, and kidney were intact, consistent with those in the control group (Fig. 7b), and no significant injury or pathological changes were detected. Hence, these data indicate that Pt^{2+}-CDs@PpIX has good biocompatibility and exerts no significant toxicity in vivo, making it a potential nanosized particle for the intracellular delivery of antitumor agents.

2.9 In vivo fluorescence imaging for determining the suitable US-exerting time

To optimize the precision of SDT in tumor treatment, we conducted in vivo imaging experiments to evaluate the tumor-targeting ability of Pt^{2+}-CDs@PpIX, which was labeled with the NIR fluorescent dye indocyanine green (ICG) and intravenously administered into BALB/c nude mice. First, we determined the appropriate time to apply US based on the results of the in vivo fluorescence imaging of the administered Pt^{2+}-CDs@PpIX. Fluorescence imaging was performed at different time points (0, 8, 24, 48, 72, and 96 h). In vivo imaging (Figs. 8a and 8b) and organ imaging (Fig. 8c) confirmed that Pt^{2+}-CDs@PpIX exhibited strong tumor-targeting capabilities through the well-documented enhanced permeability and retention (EPR) effect [59, 60]. The strongest fluorescent signal at the tumor site was detected 72 h after injection.

The fluorescence intensity of Pt^{2+}-CDs@PpIX in the liver also gradually declined, suggesting hepatic metabolism as the primary clearance pathway, consistent with most nanoparticles. This approach could reduce side effects in clinical patients [61]. Quantification of the tumor fluorescence intensity (Figs. 8a–8c; Fig. S22 in the supplementary information) revealed higher fluorescence at 24, 48, and 72 h than at 96 h. Therefore, 24, 48, and 72 h postadministration were selected as optimal time points for US application. These findings further demonstrate the strong tumor-targeting potential of Pt^{2+}-CDs@PpIX, as evidenced by autofluorescence imaging.

2.10 Antitumor efficacy of Pt^{2+}-CDs@PpIX in vivo

Building on the efficient sonodynamic performance and strong tumor-targeting ability of Pt^{2+}-CDs@PpIX, we further investigated its enhanced SDT efficacy in vivo. The treatment regimen (Fig. 8d) consisted of a low-dose administration of 3.0 mg/kg Pt^{2+}-CDs@PpIX, followed by US irradiation (50 kHz, 2.0 W/cm^2, 5 min) at 24, 48, and 72 h postinjection. After extensively evaluating the biosafety of Pt^{2+}-CDs@PpIX in vivo and in vitro, we subsequently investigated its synergistic antitumor effects.

We further evaluated the antitumor efficacy of Pt^{2+}-CDs@PpIX in a BALB/c nude mouse SMMC-7721 hepatocellular carcinoma xenograft model. Tumor-bearing nude mice with tumor volumes of approximately 70 mm^3 were randomly divided into seven groups (n=3 in each group), including group 1: control group (intravenous saline), group 2: +US (intravenous saline), group 3: Pt^{2+}-CDs@PpIX (intravenous Pt^{2+}-CDs@PpIX), group 4: Pt^{2+}-CDs+US (intravenous Pt^{2+}-CDs and exposed to US irradiation), group 5: PpIX+US (intravenous PpIX and exposed to US irradiation), group 6: CDs@PpIX+US (intravenous CDs@PpIX and exposed to US irradiation), and group 7: Pt^{2+}-CDs@PpIX+US (intravenous Pt^{2+}-CDs@PpIX and exposed to US irradiation). Figures 8e and 8f show the digital photographs of the resected tumors in each group on the last day of treatment. By comparing the weight and volume of the dissected tumors after treatment, as depicted in Figs. 8g and 8h, we found that mice treated with Pt^{2+}-CDs@PpIX+US (group 7) obtained more significant tumor suppression than mice treated in the other six groups. The trend of tumor volume changes was monitored every 3 d, which further demonstrated that the therapeutic effect of SDT has an encouraging

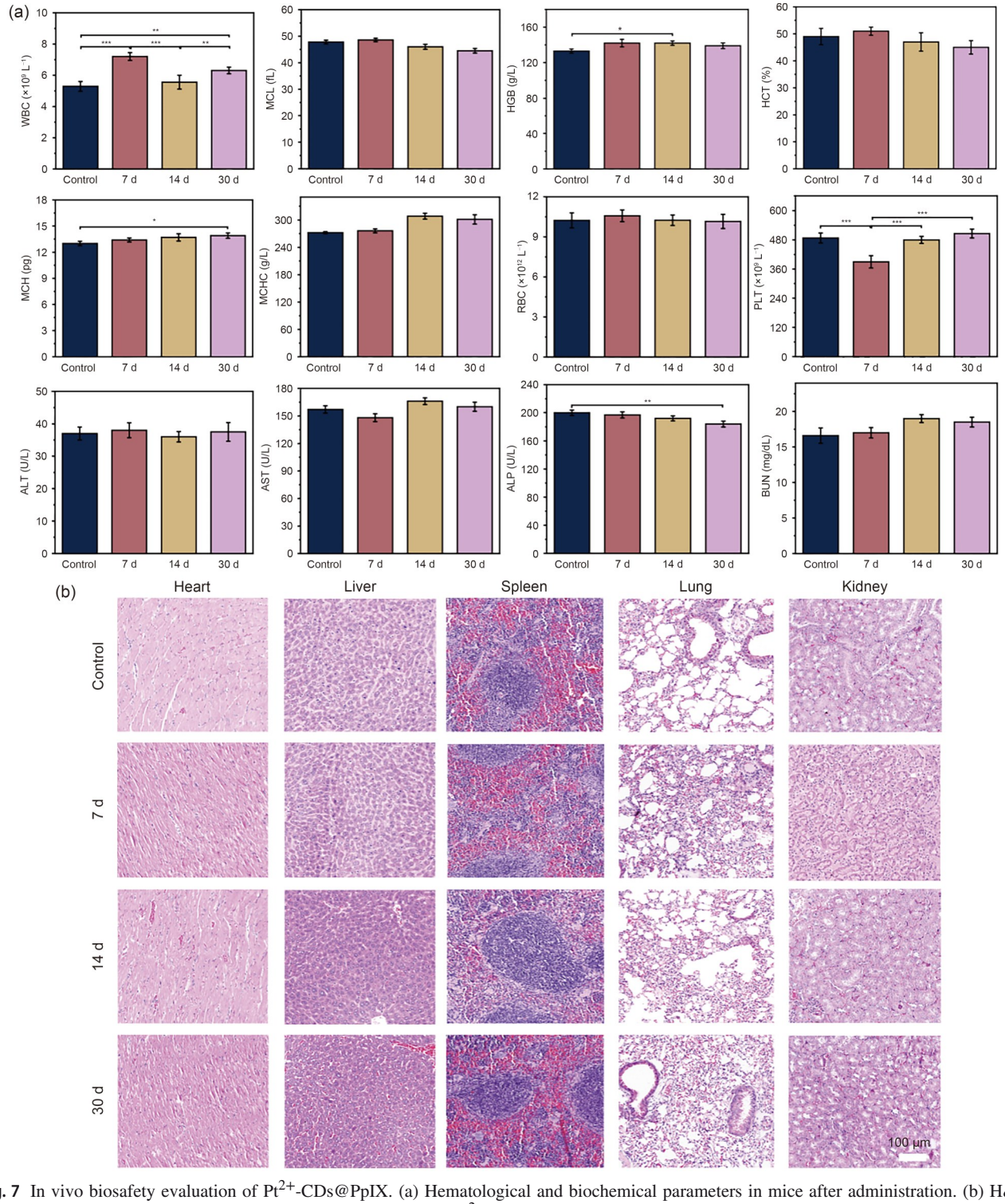

Fig. 7 In vivo biosafety evaluation of Pt^{2+}-CDs@PpIX. (a) Hematological and biochemical parameters in mice after administration. (b) H&E staining of major organs at 0, 7, 14, and 30 days postinjection of Pt^{2+}-CDs@PpIX, indicating no significant histological damage. Data in (a) are expressed as mean±standard deviation (n=3). $^{*}p<0.05$, $^{**}p<0.01$, $^{***}p<0.001$

synergistic potential to inhibit tumor growth (Fig. 8h). Throughout the 21-d treatment period, there was no significant weight loss in any group (Fig. 8i), suggesting that intravenous nanomedicine and US irradiation were well tolerated.

2.11 Immunohistochemical analysis of the tumor after Pt^{2+}-CDs@PpIX treatment

To further visualize the accumulation of ROS in the tumor tissues, we used the DCFH-DA fluorescent dye as an ROS

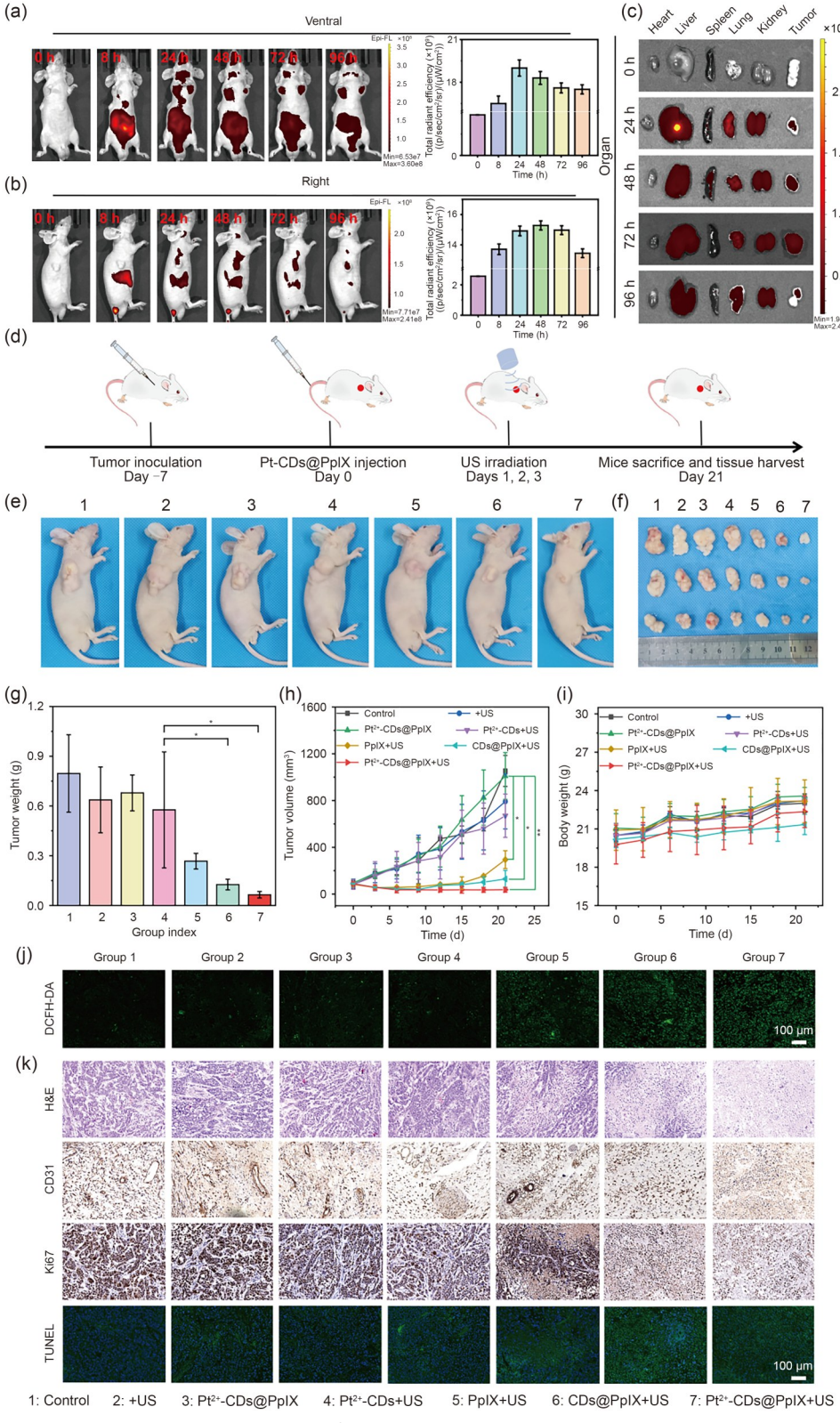

Fig. 8 In vivo biodistribution and antitumor efficacy of Pt^{2+}-CDs@PpIX in SMMC-7721 tumor-bearing mice under ultrasound irradiation. (a, b) Time-course NIR fluorescence imaging of mice injected with ICG-labeled Pt^{2+}-CDs@PpIX. (c) Ex vivo fluorescence images of major organs and tumors. (d) Schematic of SDT timeline. (e, f) Representative images of mice and tumors after 21 days. (g, h) Tumor weight and tumor growth curves. (i) Body weight variation of mice. (j) ROS levels in tumor tissues as evaluated by DCFH-DA staining. (k) H&E, CD31, Ki67, and terminal deoxynucleotidyl transferase dUTP nick-end labeling (TUNEL) staining of tumor slices. Data in (a, b, g–i) are expressed as mean± standard deviation (n=3). $^{*}p<0.05$

probe. The green fluorescence was the most significant in the Pt^{2+}-CDs@PpIX+US treatment group, suggesting that Pt^{2+}-CDs@PpIX+US could induce a large amount of ROS production in vivo (Fig. 8j). These data confirm the ideal therapeutic effect of Pt^{2+}-CDs@PpIX+US treatment to increase the degree of ROS-induced oxidative damage to tumor cells. Furthermore, H&E staining and Ki67, CD31, and terminal deoxynucleotidyl transferase dUTP nick-end labeling (TUNEL) assays were performed to evaluate the apoptotic effects in xenograft tumors. As depicted in Fig. 8k, the positive signal of apoptosis detected by H&E staining and TUNEL assay in the Pt^{2+}-CDs@PpIX+US group was stronger than that in the other groups. The tumor specimens of tumor-bearing mice in the Pt^{2+}-CDs@PpIX+US group also demonstrated different degrees of cell necrosis, such as cell atrophy, incomplete nucleus, and light staining. The tumor cells in the control and US-treated groups were closely arranged, with large and intact nuclei and deep staining. In contrast, the degree of apoptosis and necrosis of tumor cells was higher in the Pt^{2+}-CDs@PpIX+US group than in the other six groups. CD31 was expressed on the surface of vascular endothelial cells and can also be used to evaluate tumor angiogenesis [62]. As illustrated in Fig. 8k, the microvascular density of primary and distant tumors in the Pt^{2+}-CDs@PpIX+US group was significantly lower than that in the other groups. As a marker of tumor proliferation, the expression of Ki67 protein highly correlated with cell mitosis and was directly proportional to the cell proliferation capacity [63, 64]. In the control, US, and Pt^{2+}-CDs@PpIX groups, a strong dark brown color was observed in the nuclear positive signal (indicating tumor cell proliferation). The number of Ki67-positive cells in the Pt^{2+}-CDs@PpIX+US group was significantly reduced, which further confirmed that Pt^{2+}-CDs@PpIX+US could inhibit the proliferation of tumor cells. The level of Ki67 expression in the Pt^{2+}-CDs@PpIX+US treatment group was significantly lower than that in the other groups, thus indicating the improved tumor-killing ability. These immunohistochemical results are consistent with tumor growth data. Thus, SDT plays a therapeutic role in inducing apoptotic cell death, and the drug delivery system can significantly expand the killing effect of treatment, ultimately inhibiting tumor growth.

2.12 Transcriptome sequencing of tumors after Pt^{2+}-CDs@PpIX treatment

The therapeutic effects of Pt^{2+}-CDs@PpIX+US on tumors in nude mice were investigated using whole-transcriptome RNA sequencing (RNA-seq). As shown by the Venn diagram and bar chart in Fig. 9a, 1414 and 2028 differentially expressed genes (DEGs) were identified in the control and Pt^{2+}-CDs@PpIX+US groups, respectively. Compared with those in the control group, there were 149 upregulated and 1089 downregulated genes in the Pt^{2+}-CDs@PpIX+US group. Significant DEGs were selected for further analysis. The volcano plots shown in Fig. 9b depict the differential gene expression patterns, wherein red and blue indicate significantly upregulated and downregulated genes, respectively, and gray represents non-significant changes. The clustering heat maps (Fig. 9c) show that after treatment the tumors in the control and Pt^{2+}-CDs@PpIX+US groups had different gene expression profiles, indicating that different treatments produced tumors with different microenvironments.

The Kyoto Encyclopedia of Genes and Genomes (KEGG) pathway bubble charts of the DEGs are depicted in Fig. 9d. Compared with those in the control group, the p53, PI3K-Akt, TGF-β, and other signaling pathways in the Pt^{2+}-CDs@PpIX+US group were significantly affected. It is highly possible that Pt^{2+}-CDs@PpIX+US exerts therapeutic effects through these signaling pathways.

The functional evaluation of the DEGs was performed through Gene Ontology (GO) enrichment analysis of the upregulated genes (Fig. 9e), which revealed that the Pt^{2+}-CDs@PpIX+US group was primarily enriched in pathways related to the positive regulation of cell death, response to hydrogen peroxide, hydrogen peroxide catabolic process, oxygen transport, oxygen binding, peroxidase activity, and oxygen carrier activity.

As depicted in Fig. S23 (supplementary information), the results of gene set enrichment analysis (GSEA) revealed that, compared with that in the control treatment, the Pt^{2+}-CDs@PpIX+US treatment promoted processes such as hydrogen peroxide catabolic process, DNA damage response, p53 signaling pathway activation, and the positive regulation of cell death. Moreover, signal transduction pathways, including cell migration regulation, cell death, positive regulation of cell migration, and the TGF-β receptor signaling pathway, were suppressed.

To summarize, RNA-seq further confirmed that the Pt^{2+}-CDs@PpIX+US nanoplatform improved ROS production, resulting in cell apoptosis and also inhibiting cell migration and proliferation, thereby clarifying its underlying mechanism.

The practical translation of Pt^{2+}-CDs@PpIX into clinical applications depends on its scalability, biosafety, and regulatory compliance. Benefiting from a relatively simple and reproducible synthesis process, this nanoplatform has potential for large-scale production. Furthermore, its favorable biocompatibility and efficient tumor-targeting capabilities support its translational prospects. However, it is necessary to carefully address challenges such as long-term in vivo biosafety, manufacturing consistency, and meeting stringent regulatory standards. Future studies must focus on optimizing formulation stability, conducting comprehensive

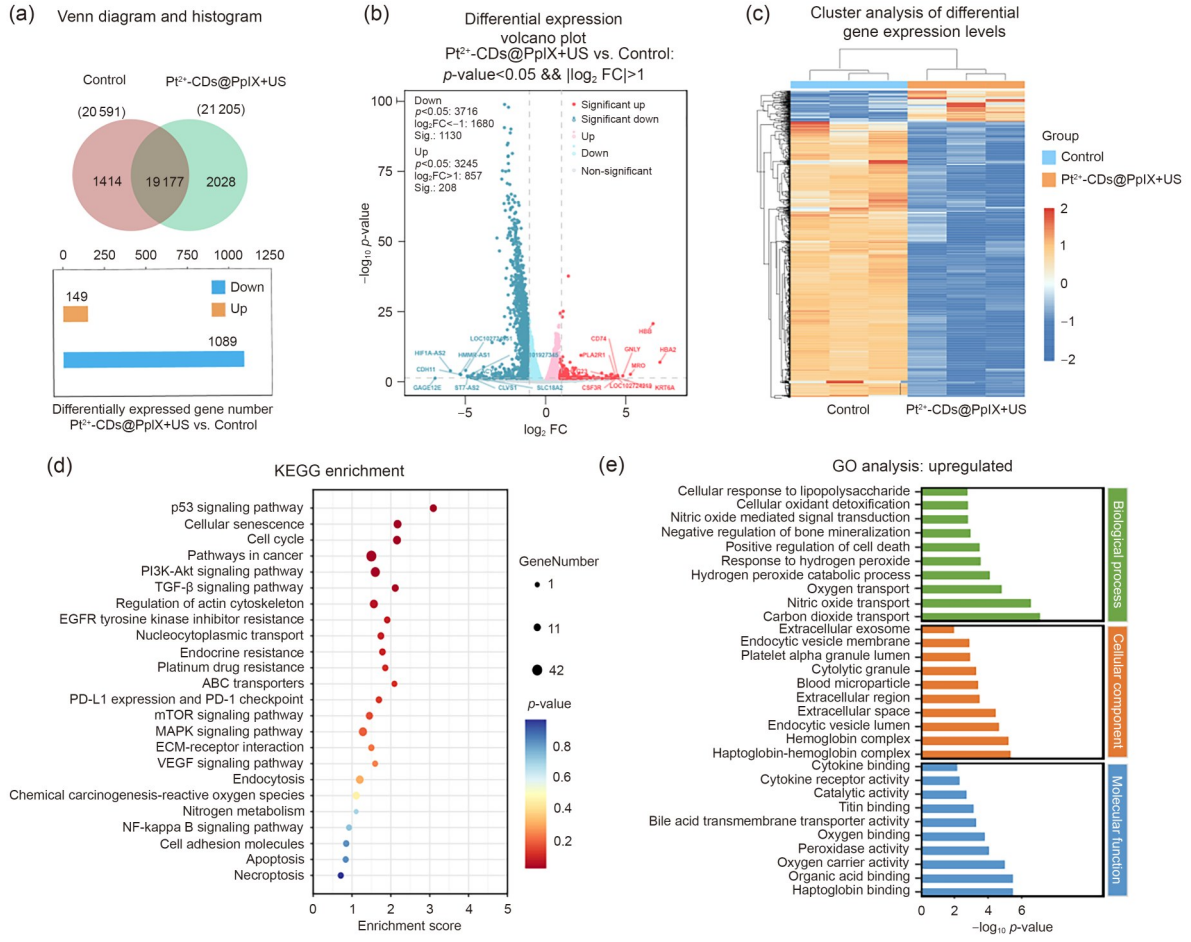

Fig. 9 Transcriptomic analysis of differential gene expression posttreatment. (a) Venn diagram and histogram of DEGs between the control and Pt^{2+}-CDs@PpIX+US groups. (b) Volcano plot depicting significantly upregulated/downregulated DEGs. (c) Heat map of the top DEGs in both groups. (d) KEGG pathway enrichment analysis of the DEGs. (e) GO enrichment of upregulated genes in the Pt^{2+}-CDs@PpIX+US group

pharmacokinetic and toxicological evaluations, and exploring combination strategies to accelerate clinical adoption.

3 Conclusions

We developed a novel nanoplatform (Pt^{2+}-CDs@PpIX) that enhances ROS generation by targeting the nucleolus and simultaneously weakens the ROS defense system by depleting GSH levels. The Pt^{2+}-CDs@PpIX composite not only demonstrated a strong capability to deplete GSH levels, enabling the fluorescence imaging of intracellular GSH, but also allowed for the screening of cancer cells and normal cells with varying GSH levels. Immunofluorescence and qRT-PCR experiments demonstrated that the Pt^{2+}-CDs@PpIX+US SDT could promote DNA oxidation damage. After treatment with Pt^{2+}-CDs@PpIX, the cells displayed remarkable antitumor activities. Moreover, Pt^{2+}-CDs@PpIX+US treatment significantly inhibited the migration, invasion, and colony formation of SMMC-7721 cells in the 3DM-7721 model. Xenograft mouse models confirmed the in vivo antitumor efficacy of the Pt^{2+}-CDs@PpIX+US nanotherapeutic system. During treatment, intravenous injection of Pt^{2+}-CDs@PpIX followed by US irradiation effectively suppressed tumor growth without noticeable toxicity to the mice, resulting in a remarkable therapeutic outcome. Both in vitro and in vivo experiments indicated that this probe can release drugs in the acidic tumor microenvironment (TME), deliver drugs to target cells via CDs, and significantly improve the efficacy of SDT by depleting intracellular GSH levels. Therefore, our study suggests that the Pt^{2+}-CDs@PpIX+US-based nanoplatform has a broad potential for cancer treatment and a wide range of biomedical applications.

4 Experimental section

4.1 Materials and characterization

The following materials were provided by Sinopharm Chemical Reagent Company (Beijing, China): L-cysteine,

m-phenylenediamine (mPD), PpIX, hydrogen hexachloroplatinate hexahydrate (H_2PtCl_6, $6H_2O$, 99.0%), penicillin-streptomycin, porcine skin gelatin, phenyl-(2,4,6-trimethylbenzoyl)phosphonate lithium (LAP, a photoinitiator, PI), dimethyl sulfoxide (DMSO), and N,N-dimethylformamide (DMF). Mack Ward Biologics Co., Ltd. (Nanjing, China) supplied 1-hydroxybenzotriazole (HOBt), N,N′-dicyclohexylcarbodiimide (DCC), phosphate-buffered saline (PBS), Dulbecco's modified Eagle medium (DMEM; pH 7.4 or 6.8), fetal bovine serum (FBS), and other cell culture reagents. Chuangsai Technology Co., Ltd. (Shanghai, China) provided the dialysis tubing MD34 (with a molecular weight cutoff of 8–14 kDa). Abclonal Technology (Wuhan, China) supplied 8-oxonine (8-oxoG), AFP, proliferative marker protein Ki-67 (Ki67), and albumin (ALB). The CCK-8 and DAPI were obtained from BestBio (Shanghai, China). Normal cells (LO2), HUVECs, and human hepatocellular carcinoma cells (SMMC-7721, HepG2) were provided by Wuhan Purcell Life Science & Technology Co., Ltd., China. Because all reagents were of analytical quality, they did not require additional purification. Deionized water supplied by Shanghai Yiheng Scientific Instrument Co., Ltd. (Shanghai, China) was used for the UPT-II ultrapure water system.

The morphological features of CDs were evaluated under a high-resolution transmission electron microscope (JEOL-2100F, Tokyo, Japan). A UV–Vis spectrophotometer (METASH UV-8000, Shanghai, China) with a wavelength range of 190–1200 nm was used to produce the absorption spectra. XRD measurements were performed using the Rigaku 18 kW D/max-2550. An FLS-980 fluorescence spectrophotometer (Edinburgh Instruments, UK) was used for determining the fluorescence spectra. Dynamic light scattering (DLS) was used for measuring the zeta potential of the system and the particle size (Malvern ZS90, UK). Cell morphology was recorded using a Cytation5 Imaging Reader (BioTek, USA). The 3D bioprinter employed in this study was manufactured by Envision TEC GmbH. A spectrophotometer (NanoDrop OneC, Thermo Scientific, USA) was used for measuring the quantity and quality of RNA. RNA was transformed into complementary DNA (cDNA) using Takara's PrimeScript™ RT Master Mix. RT-PCR analysis was performed using the Biosystems™ QuantStudio™ 6 Flex RT-PCR system and Premix Ex Taq™ II (Takara, Japan).

4.2 Preparation of Pt^{2+}-CDs@PpIX

The CDs were prepared according to previous studies [53, 65]. Briefly, 30 mL of deionized water was used to dissolve 0.3 g of mPD and 0.675 g of L-cysteine, which were then well combined and swirled. The combined liquid was added to a muffle furnace, which was then placed inside a box-type resistance furnace. The temperature inside the box-type resistance furnace was adjusted to 160 °C, and after 10 h of reaction, the CDs were produced. Subsequently, 1 mL of K_2PtCl_6 aqueous solution was gradually added to 1 mL of the previously prepared aqueous CD solution, and the mass ratio of K_2PtCl_6 to CDs was adjusted to 1:30–1:1. After 30 min of incubation at 25 °C, centrifugation at 10,000 r/min for 5 min, and centrifugation three times, the Pt^{2+}-CDs were obtained.

Next, 2 mg of PpIX, 2.69 mg of DCC, and 1.76 mg of HOBt were dissolved in 5 mL of DMSO and reacted at room temperature for 6 h to activate the carboxyl groups of PpIX. Then, 4 mg of Pt^{2+}-CDs was dissolved in 5 mL of DMSO and mixed with the activated PpIX solution. The mixture was stirred magnetically at 25 °C in the dark for 12 h and then centrifuged at 4000 r/min for 5 min, followed by dialysis against water using a membrane with a molecular weight cutoff of 3500 Da for 24 h to remove excess PpIX. It was then freeze-dried to obtain the drug-loaded system Pt^{2+}-CDs@PpIX. The prepared CDs, Pt^{2+}-CDs, and Pt^{2+}-CDs@PpIX were characterized by TEM, UV absorption spectra, fluorescence spectra, zeta potential, and hydration radius.

Before using the abovementioned PpIX and Pt^{2+}-CDs drug dosages, we calculated the maximum drug-loading rate using the following experimental design: different mass ratios of Pt^{2+}-CDs to PpIX (0.5, 1.0, 1.5, 2.0, 2.5, 3.0) were used for synthesizing the abovementioned Pt^{2+}-CDs@PpIX, the solution outside the dialysis bag was taken after the completion of the dialysis, and the UV absorbance of PpIX at 400 nm was measured. According to the calibration curve of the concentration and absorbance of PpIX, the optimal amount of PpIX linked to Pt^{2+}-CDs was obtained, and the highest drug-loading rate was calculated. In Eq. (1), A_0 is the amount of the drug bound and A_1 is the amount of the total drug added.

$$r_{\text{DrugLoading}} = A_0/A_1 \times 100\%. \quad (1)$$

4.3 In vitro coagulation assay

Fresh anticoagulated human blood was obtained from the First Hospital of Shanxi Medical University, Shanxi Province, China. Whole blood was diluted with PBS at a 1:1 ratio. In a 24-well plate, 1 mL of PBS was mixed with 0.05 mL of the diluted blood, followed by the addition of 60 μg/mL of each of the following samples: CDs, PpIX, Pt^{2+}-CDs, Pt^{2+}-CDs+GSH, and Pt^{2+}-CDs@PpIX. The control group received an equal volume of deionized water. After incubation at 37 °C for 1 h, 100 μL of the solution from each well was transferred to a 96-well plate, and the absorbance was measured at 540 nm. The BCI was calculated using the following formula:

$$\text{BCI} = (E-G)/(F-G) \times 100\%, \quad (2)$$

where E is the absorbance of the experimental group, F is the absorbance of the control group, and G is the absorbance of deionized water.

4.4 Sensitivity and selectivity of Pt^{2+}-CDs for GSH detection

For detecting sensitivity, 1 mL of Pt^{2+}-CDs (60 μg/mL) was transferred into each of nine centrifuge tubes. Then 50-μL samples of GSH solution at concentrations of 0, 1, 2, 3, 4, 5, 6, 7, and 8 mmol/L were added to the abovementioned nine centrifuge tubes. The reaction system was stirred evenly using a magnetic stirrer, and after 30 s, the fluorescence spectrum of the abovementioned solutions was measured under an excitation wavelength of 400 nm.

For detecting selectivity, 1 mL of Pt^{2+}-CDs (60 μg/mL) was transferred into each of 11 centrifuge tubes, and then different electrolytes and biomolecules (deionized water, AA, BSA, PBS, GSH, NaCl, KCl, $MgCl_2$, L-Thr, Arg, and Asp) at a concentration of 8 mmol/L were respectively added to these tubes. The reaction system was stirred evenly using a magnetic stirrer, and after 30 s, the solution was sequentially measured under an excitation wavelength of 400 nm.

GSH (1 mmol/L) was mixed with the Pt^{2+}-CDs@PpIX solution. Then, 50 μL of the mixed solution was mixed with PBS (450 μL) and DTNB (2 μL) at different time points. After centrifugation (10,000 r/min, 5 min) to remove Pt^{2+}-CDs@PpIX, the absorbance of the supernatant was measured using a UV–Vis spectrophotometer (412 nm).

4.5 Quantitative analysis of ROS generation

To detect the superoxide anion radical $'O_2$, DPBF (1 mg/mL, 20 μL) was added to Pt^{2+}-CDs, PpIX, and Pt^{2+}-CDs@PpIX solutions. The absorbance of the mixed solution was measured at 420 nm to quantify the oxidation rate of DPBF under Pt^{2+}-CDs@PpIX+US (at different time points of 0, 1, 2, 3, 4, and 5 min).

4.6 Cytotoxicity and cell imaging

SMMC-7721 cells were seeded in 24-well culture plates and cultured under sterile conditions for 24 h. The cell culture medium was discarded, the cells were washed three times in PBS, and 1 mL of fresh medium was added. Then, the SMMC-7721 cells were supplemented with different concentrations of CDs, Pt^{2+}-CDs, PpIX, CDs@PpIX, and Pt^{2+}-CDs@PpIX (0, 20, 40, 60, 80, and 100 μg/mL) and exposed to US radiation (1.5 W/cm^2) for 10 min, after which the viability of CCK-8 cells without irradiation was statistically analyzed.

Then, the samples were stained as follows: 5 μL of CDs (60 μg/mL), Pt^{2+}-CDs (60 μg/mL), and Pt^{2+}-CDs@PpIX (60 μg/mL) solutions were added to the abovementioned culture plate containing the cells, incubated at 37 °C for 20 min, and the changes in fluorescence of the cells were observed under a fluorescence microscope to obtain the fluorescence imaging after incubation with different cells. Using DTNB as a GSH indicator, we measured the time of GSH depletion in Pt^{2+}-CDs and Pt^{2+}-CDs@PpIX solutions and detected the UV absorption spectrum of the solutions at different time points. To the abovementioned culture plate containing the cells, 5 μL of CDs, PpIX, CDs@PpIX, and Pt^{2+}-CDs@PpIX solutions were added and incubated at 37 °C for 20 min, after which the nuclear entry of the drugs was observed under a fluorescence microscope. For the quantitative analysis of fluorescence intensity, the cells were digested and resuspended in PBS. Flow cytometry was used for quantifying the intracellular signal.

4.7 Extracorporeal SDT

SMMC-7721 cells were seeded in 24-well culture plates and cultured under sterile conditions for 24 h. After discarding the cell culture medium, the cells were washed three times with PBS and then incubated with 1 mL of fresh medium. The experimental groups were set up as follows: group 1 (control), group 2 (+US), group 3 (Pt^{2+}-CDs@PpIX), group 4 (Pt^{2+}-CDs+US), group 5 (PpIX+US), group 6 (CDs@PpIX+US), and group 7 (Pt^{2+}-CDs@PpIX+US). All treatments were prepared in DMSO and diluted to a final concentration of 1 mg/mL; 5 μL of the abovementioned solution was added to the culture plate containing the cells and incubated at 37 °C for 20 min, and groups 2, 4, 5, 6, and 7 were exposed to US radiation (1.5 W/cm^2) using a US instrument for 10 min, after which the survival rate of CCK-8 cells was analyzed in each group. After different treatments, SMMC-7721 cells were costained with live/dead dyes (PI and Calcein-AM) for fluorescence imaging. SMMC-7721 cells were costained with DAPI and DCFH-DA (ROS) after various treatments.

4.8 Application of the nanoplatform in the 3D tumor microenvironment model (3DM-7721)

The 3DM-7721 model was constructed based on previous research [66]. For preparing the core printing fraction, a mixed solution of 10%/6% GelMA/gelatin was prepared. SMMC-7721 cells (density of 5×10^5 cells/mL) were mixed with the 10%/6% GelMA/gelatin solution to generate a cell suspension. Then, 3 mL of the cell/biomaterial mixture was pumped into a sterile syringe equipped with a 30G needle (160 μm) for defoaming. After degassing, it was placed in a

3D printer with a barrel temperature of 25 °C and left for 30 min. The printing process was carried out under the following parameters: barrel temperature at 25 °C, platform temperature at 0 °C, nozzle diameter of 0.128 mm, printing pressure of 1 bar (1 bar=100 kPa), and printing speed of 13.0 mm/s. Both front and back flow delays were set to 0 s, with an interlayer waiting time of 15 s to allow for photo-crosslinking (performed at approximately 405 nm, 20 W/cm^2). The minimum printable line length was 0.4 mm, and the material density was set to 1.00 g/cm^3. A 35-mm-diameter Petri dish was used to collect the printed structures. The printed model was supplemented with 2 mL of preprepared medium and transferred to a 37 °C, 5% CO_2 incubator for incubation. The medium was changed every 2 d.

Regarding the construction of the peripheral model, a high-precision UV-curing 3D printer was used to print a resin-cured ring model. The printed 3DM-7721 model was placed in the middle of the curing ring, and 300 μL of the 10%/3% GelMA/gelatin mixed solution was added to the curing ring to wrap the printed 3DM-7721 model. The model was then cross-linked and cured with UV blue light (approximately 405 nm, 20 W/cm^2) for 15 s to generate the 3DM-7721 model. The 3DM-7721 model was incubated in a 37 °C, 5% CO_2 incubator with 2 mL of preprepared medium. The medium was changed every 2 d.

The constructed TME model was used to assess the application and efficacy of the drug-loading system. Solutions from groups 1 (control), 2 (+US), 3 (Pt^{2+}-CDs@PpIX), 4 (Pt^{2+}-CDs+US), 5 (PpIX+US), 6 (CDs@PpIX+US), and 7 (Pt^{2+}-CDs@PpIX+US) were diluted with DMSO to a concentration of 100 μg/mL. Then, 5 μL of the abovementioned solution was added to the culture plate containing the 3DM-7721 model, incubated at 37 °C for 20 min, and groups 2, 4, 5, 6, and 7 were subjected to US (1.5 W/cm^2) sonication using a US instrument for 10 min. After different treatments, SMMC-7721 cells were costained with live/dead dyes (PI and Calcein-AM) for fluorescence imaging. SMMC-7721 cells were also costained with DAPI and DCFH-DA (ROS) after various treatments.

4.9 Effects of Pt^{2+}-CDs@PpIX on migration, invasion, and colony formation

Collagenase II was added to the medium to degrade (2 mg/mL, 0.5 h) the treated 3DM-7721 model to obtain treated SMMC-7721 cells. The sample was filtered using a 70-μm filter to avoid the formation of clumps or particles of undigested polymers. The suspension was centrifuged at 2000 r/min for 5 min, and the supernatant was discarded to collect the obtained SMMC-7721 cells.

Scratch experiment: Horizontal lines were evenly drawn using a marker pen across the back of a 12-well plate, ensuring that each well had at least three lines. The SMMC-7721 cells extracted from the above-described 3DM-7721 model were seeded in the 12-well plate. Cells were cultured at 37 °C and 5% CO_2 for 24 h. The next day, using a 200-μL pipette tip, vertical scratches were made along the lines on the back of the plate, ensuring that the pipette tip was perpendicular and not tilted. Cells were washed with PBS three times to remove any detached cells, serum-free media were added, and then the marker pen lines on the back of the plate were removed. The cells were incubated for 1 h with the following different treatments: control, +US, Pt^{2+}-CDs@PpIX, Pt^{2+}-CDs+US, PpIX+US, CDs@PpIX+US, and Pt^{2+}-CDs@PpIX+US. After incubation, the cells were exposed to US radiation (1 MHz, 1.5 W/cm^2, 10 min). The scratched area after laser irradiation for 0, 12, and 24 h was photographed.

Transwell invasion experiment: SMMC-7721 cells were obtained separately from the 3DM-7721 model after treatment in different groups (control, +US, Pt^{2+}-CDs@PpIX, Pt^{2+}-CDs+US, PpIX+US, CDs@PpIX+US, and Pt^{2+}-CDs@PpIX+US). The excess Matrigel fluid was gently aspirated from the upper chamber, and 200 μL (5×10^4 cells/mL) of the treated SMMC-7721 cell suspension was added to resuspend the treated SMMC-7721 cell suspension using serum-free medium, after which 500 μL of complete medium was added to the lower chamber. After 24 h, the medium of the upper and lower chambers was discarded, both chambers were washed three times each with PBS, and the noninvasive cells in the upper chamber were wiped off with a cotton swab. Cells were fixed with 4% paraformaldehyde for 20 min at room temperature. Then, 500 μL of 0.1% crystal violet-stained cells was added to the lower chamber and incubated for 30 min, and the staining solution was washed with PBS. Images were acquired using a microplate reader.

Colony formation capacity experiment: SMMC-7721 cells were obtained separately from the 3DM-7721 model after treatment in different groups (control, +US, Pt^{2+}-CDs@PpIX, Pt^{2+}-CDs+US, PpIX+US, CDs@PpIX+US, and Pt^{2+}-CDs@PpIX+US), and the single-cell suspension (2.5×10^3 cells/mL, 2 mL/well) of each group was seeded into a 6-well plate and incubated for 14 d, with the medium being changed every 3 d. After two washes with PBS, the cells were fixed with 4% paraformaldehyde for 20 min at room temperature. The cells were then stained with 0.1% crystal violet for 30 min. Images were acquired using a microplate reader.

4.10 Protein and mRNA expression

SMMC-7721 cells were seeded in 24-well plates and incubated for 24 h under sterile conditions. The cell culture medium was discarded, the cells were washed three times in

PBS, and 1 mL of fresh medium was added. Samples from groups 1 (control), 2 (+US), 3 (Pt^{2+}-CDs@PpIX), 4 (Pt^{2+}-CDs+US), 5 (PpIX+US), 6 (CDs@PpIX+US), and 7 (Pt^{2+}-CDs@PpIX+US) were diluted with DMSO to a concentration of 1 mg/mL. Then, 5 μL of the abovementioned solution was added to the cell-containing culture plates and incubated at 37 °C for 20 min, and groups 2, 4, 5, 6, and 7 were exposed to US radiation (1.5 W/cm^2) for 10 min using a US instrument. These cells were cultured for 2 d and washed three times in PBS, after which immunofluorescence staining was performed to detect 8-oxoG, 53BP1, AFP, EpCAM, Ki67, and ALB proteins. Finally, fluorescence images were obtained using a Cytation5 imaging reader.

To analyze gene expression, cells were collected after digestion with trypsin, treated with frozen TRIzol^{TM} reagent, and allowed to sit for 15 min with intermittent shaking to isolate total RNA. cDNA was synthesized from the extracted RNA using the PrimeScript^{TM} RT Master Mix kit according to the manufacturer's instructions. qRT-PCR was performed with TB Green^{TM} Premix Ex Taq^{TM} II (Takara) using the Applied Biosystems QuantStudio 6 Flex real-time PCR system. Real-time PCR was performed to detect the mRNA expression of SMMC-7721 genes, including *Ki67*, *AFP*, *CD133*, *EpCAM*, *TGF-β*, *CD24*, *Bcl-2*, and *53BP1*. The relative gene expression levels of these genes were calculated using the $2^{-\Delta\Delta C_T}$ method [33]. The antibody information and primer sequences are shown in Tables S1 and S2 (supplementary information). Gene expression was normalized to recombinant human β-actin (*β-actin*), and all qRT-PCR analyses were performed for 40 cycles. Data are expressed as mean±standard deviation (n=3).

4.11 Western blot analysis

Cell treatment and protein extraction: SMMC-7721 cells were seeded in 6-well plates at a density of 2.5×10^5 cells/well and allowed to adhere. After attachment, the cells were treated with the following experimental groups: control (untreated), +US (US only), Pt^{2+}-CDs@PpIX (nanoplatform only), Pt^{2+}-CDs+US, PpIX+US, CDs@PpIX+US, and Pt^{2+}-CDs@PpIX+US. Then, the cells were incubated at 37 °C for 20 min, after which groups 2, 4, 5, 6, and 7 were exposed to US radiation (1.5 W/cm^2) for 10 min. Next, the medium was aspirated, and cells were gently washed three times with ice-cold PBS to remove the residual drugs and medium impurities. Total protein was extracted using radioimmunoprecipitation assay (RIPA) lysis buffer supplemented with phenylmethylsulfonyl fluoride (PMSF; 1:100, volume ratio), followed by incubation for 20 min at 4 °C. The lysates were then transferred to 1.5-mL microcentrifuge tubes and centrifuged at 13,000 r/min for 20 min at 4 °C. The resulting supernatant was collected, mixed with 5× sodium dodecyl sulfate (SDS) loading buffer (1:4 ratio), and denatured by boiling at 100 °C for 10 min with intermittent vortexing.

Gel preparation and electrophoresis: SDS-PAGE gels (separation and stacking gels) were prepared according to the Elabscience® SDS-PAGE Gel Preparation Kit protocol. After polymerization, denatured protein samples (20 μL) were loaded into each lane. Electrophoresis was performed in a 1× SDS running buffer under optimized voltage and current conditions.

Protein transfer and blocking: After electrophoresis, the proteins were transferred onto polyvinylidene fluoride (PVDF) membranes at a constant current of 200 mA for 1.5 h in a 1× transfer buffer. To minimize the background, the membranes were blocked with 5% nonfat milk in PBST (PBS+0.1% Tween-20) for 2 h at room temperature with gentle shaking.

Antibody incubation and detection: Membranes were incubated with diluted primary antibodies (refer to Table S3 in the supplementary information for concentrations) overnight at 4 °C on a shaker, after which they were washed three times with tris-buffered saline with Tween 20 (TBST) (10 min per wash) to remove unbound antibodies. Then, the membranes were incubated with horseradish peroxidase (HRP)-conjugated goat antirabbit immunoglobulin G (IgG; 1:5000 dilution) for 2 h at room temperature in the dark. After washing three times with TBST (10 min each), protein bands were visualized using the enhanced chemiluminescence (ECL) chemiluminescence substrate and imaged with a chemiluminescence gel documentation system. Band intensities were analyzed using the ImageJ software, and relative protein expression levels were compared across treatment groups.

4.12 Animal and tumor models

In vivo tumorigenicity assays were performed using BALB/c nude mice (male, aged 5–6 weeks, weighing 18–25 g). The 3DM-7721 model (containing 1×10^6 SMMC-7721 cells, 1×10^6 human dermal fibroblast (HDF) cells, 1.5×10^6 HUVECs) was prepared as described earlier and cultured in medium for 7 d. Collagenase was added to the medium for degradation (2 mg/mL, 0.5 h) and filtered through a 70-μm filter to avoid clumps or particles of undigested polymer. The supernatant was discarded after centrifuging the suspension for 5 min at 2000 r/min. ABW® Matrigel was mixed with PBS in a 1:1 ratio (at 4 °C), and then cells were added to form a suspension. The cell suspension (100 μL/mouse) was injected into the armpit of nude mice (four mice per model) using a precooled syringe (precooled at 4 °C). After waking up, they were housed in specific pathogen-free (SPF) animal cages with free access to water and food. The tumor volume was measured using vernier

calipers and calculated as 1/2×width^2×length. Mice can be used for further experiments after the tumor volume reaches approximately 80–100 mm^3.

4.13 In vivo fluorescence imaging and biodistribution

The Pt^{2+}-CDs@PpIX solution was diluted with DMSO to a concentration of 1 mg/mL. To label Pt^{2+}-CDs@PpIX, 20 μg/mL of indocyanine green (ICG) was vigorously stirred in DMSO for 24 h and then assembled onto the surface of Pt^{2+}-CDs@PpIX. After stirring, the unassembled ICG was removed by centrifugation at 10,000 r/min for 10 min. The resulting solution was gradually diluted with NaCl to reduce the proportion of DMSO to 10%. The ICG-labeled Pt^{2+}-CDs@PpIX was then intravenously injected into SMMC-7721 tumor-bearing mice for NIR fluorescence imaging. At different time points (0, 8, 24, 48, 72, and 96 h), in vivo NIR fluorescence imaging was performed using the IVIS Lumina II in vivo imaging system (PerkinElmer, USA). The excitation wavelength was 745 nm, and the collection wavelength was 820 nm.

The in vivo biocompatibility test was as follows: Pt^{2+}-CDs@PpIX (3 mg/kg) was injected intravenously into healthy BALB/c mice. On Days 1, 7, 14, and 30 after dosing, blood was collected to evaluate biosafety in mice by routine blood testing. The major organs of mice (heart, liver, spleen, lungs, and kidneys) were extracted and paraffin-embedded, and sections were subjected to H&E staining to examine the toxicity of Pt^{2+}-CDs@PpIX in vivo.

4.14 In vivo antitumor therapy

Mice with subcutaneous SMMC-7721 tumors were randomly divided into seven groups (n=3) as follows: group 1 (control), group 2 (+US), group 3 (Pt^{2+}-CDs@PpIX), group 4 (Pt^{2+}-CDs+US), group 5 (PpIX+US), group 6 (CDs@PpIX+US), and group 7 (Pt^{2+}-CDs@PpIX+US). Groups 1 and 2 were intravenously injected with NaCl solution. Groups 3–7 received intravenous injections (100 μL) of different formulations at a concentration of 100 μg/mL as follows: group 3, Pt^{2+}-CDs@PpIX; group 4, Pt^{2+}-CDs; group 5, PpIX; group 6, CDs@PpIX; group 7, Pt^{2+}-CDs@PpIX. US irradiation (1.5 W/cm^2, 10 min) was applied at 24, 48, and 72 h postinjection. Tumor volumes and mouse body weights were determined every 3 d for the 21 d of growth (Days 0, 3, 6, 9, 12, 15, 18, and 21). Nude mice were sacrificed by cervical dislocation after 21 d, and the tumor was removed, photographed, and weighed. The tumor specimen was cut into 5-μm-thick slices to prepare samples.

To further explore the efficacy of different treatment modalities, paraffin-embedded sections were obtained from the tumor tissues, and their apoptosis response was evaluated by TUNEL staining. H&E, CD31, and Ki67 staining were performed to evaluate the efficacy of the photodynamic combination therapy on the tumor tissues. The antibody information is listed in Table S4 (supplementary information).

4.15 RNA sequencing and bioinformation analysis

Transcriptome sequencing was performed on tumors of the control and Pt^{2+}-CDs@PpIX groups after treatment. Total RNA was isolated from tumor tissues created in nude mice and then quantified. Three technical replicates of RNA sequencing were used in the analysis, which was performed by OE Biotech Co., Ltd., Shanghai, China. The tumor tissues of the three models were analyzed using DESeq2 for differential expression. Significant DEGs were deemed to have a Q value of <0.05 and twofold changes as their thresholds. Using the OECloud platform (https://cloud.oebiotech.com/task/), heat maps and volcanic maps were generated using the R software. R (v3.2.0) was used to screen for significant enrichment items after using the hypergeometric distribution approach to perform the GO enrichment analysis of DEGs. The GSEA tool was used to perform gene set enrichment analysis.

4.16 Statistical analysis

Statistical Package for the Social Sciences (SPSS) 17.0 was used to perform one-way analysis of variance on all data. Data were expressed as mean±standard deviation. $^{*}p<0.05$, $^{**}p<0.01$, and $^{***}p<0.001$ indicated statistical significance.

Supplementary Information The online version contains supplementary material available at https://doi.org/10.1631/bdm.2500021.

Acknowledgements This work was supported by the National Natural Science Foundation of China (No. 62031022), the Shanxi Provincial Basic Research Project (Nos. 202103021221006 and 20210302123040), the Scientific and Technological Innovation Programs of Higher Education Institutions in Shanxi (No. 2021L044), the Key R&D Program of Shanxi Province (No. 202302130501006), and the Shanxi–Zheda Institute of Advanced Materials and Chemical Engineering (No. 2022SX-TD026).

Author contributions XYW participated in conceptualization, validation, methodology, formal analysis, investigation, and writing of the original draft. LTZ, ML, RC, and YFX were involved in methodology. JMW and PG were involved in validation. LQC was involved in writing—review & editing. ZXL was involved in supervision, conceptualization, writing—review & editing, and funding acquisition. DH was involved in formal analysis and writing—review & editing. SBS contributed to conceptualization, funding acquisition, supervision, and writing—review & editing.

Declarations

Conflict of interest The authors declare that they have no conflict of interest.

Ethical approval All animal procedures were approved by the Animal Ethics Committee of the First Hospital of Shanxi Medical University and were conducted in compliance with guidelines set forth by the university for the care and use of laboratory animals (license number: SYXK (Jin) 2018-0001).

Data availability The data that support the findings of this study are available from the corresponding authors upon reasonable request.

References

1. Son S, Kim JH, Wang XW et al (2020) Multifunctional sonosensitizers in sonodynamic cancer therapy. Chem Soc Rev 49(11): 3244–3261. https://doi.org/10.1039/C9CS00648F
2. Canavese G, Ancona A, Racca L et al (2018) Nanoparticle-assisted ultrasound: a special focus on sonodynamic therapy against cancer. Chem Eng J 340:155–172. https://doi.org/10.1016/j.cej.2018.01.060
3. Liang S, Deng XR, Ma PA et al (2020) Recent advances in nanomaterial-assisted combinational sonodynamic cancer therapy. Adv Mater 32(47):2003214. https://doi.org/10.1002/adma.202003214
4. Wang ZZ, Zhang Y, Ju EG et al (2018) Biomimetic nanoflowers by self-assembly of nanozymes to induce intracellular oxidative damage against hypoxic tumors. Nat Commun 9(1):3334. https://doi.org/10.1038/s41467-018-05798-x
5. Li BY, Peng WQ, Liu Y et al (2023) HIGD1A links SIRT1 activity to adipose browning by inhibiting the ROS/DNA damage pathway. Cell Rep 42(7):112731. https://doi.org/10.1016/j.celrep.2023.112731
6. Geng BJ, Xu S, Li P et al (2022) Platinum crosslinked carbon Dot@TiO_{2-x} p-n junctions for relapse-free sonodynamic tumor eradication via high-yield ROS and GSH depletion. Small 18(6): e2103528. https://doi.org/10.1002/smll.202103528
7. Jing XN, Xu YZ, Liu DM et al (2019) Intelligent nanoflowers: a full tumor microenvironment-responsive multimodal cancer theranostic nanoplatform. Nanoscale 11(33):15508-15518. https://doi.org/10.1039/c9nr04768a
8. An J, Hu YG, Cheng K et al (2020) ROS-augmented and tumor-microenvironment responsive biodegradable nanoplatform for enhancing chemo-sonodynamic therapy. Biomaterials 234:119761. https://doi.org/10.1016/j.biomaterials.2020.119761
9. González-Garzón AC, Ramón-Ugalde JP, Ambríz-García DA et al (2023) Resveratrol reduces ROS by increasing GSH in vitrified sheep embryos. Animals 13(23):3602. https://doi.org/10.3390/ani13233602
10. Niu BY, Liao KX, Zhou YX et al (2021) Application of glutathione depletion in cancer therapy: enhanced ROS-based therapy, ferroptosis, and chemotherapy. Biomaterials 277:121110. https://doi.org/10.1016/j.biomaterials.2021.121110
11. Yang S, Wong KH, Hua P et al (2022) ROS-responsive fluorinated polyethyleneimine vector to co-deliver shMTHFD2 and shGPX4 plasmids induces ferroptosis and apoptosis for cancer therapy. Acta Biomater 140:492–505. https://doi.org/10.1016/j.actbio.2021.11.042
12. Yang XZ, Du XJ, Liu Y et al (2014) Rational design of polyion complex nanoparticles to overcome cisplatin resistance in cancer therapy. Adv Mater 26(6):931–936. https://doi.org/10.1002/adma.201303360
13. Han K, Zhang WY, Zhang J et al (2016) Acidity-triggered tumor-targeted chimeric peptide for enhanced intra-nuclear photodynamic therapy. Adv Funct Mater 26(24):4351–4361. https://doi.org/10.1002/adfm.201600170
14. Peng HB, Tang J, Zheng R et al (2017) Nuclear-targeted multifunctional magnetic nanoparticles for photothermal therapy. Adv Healthc Mater 6(7):1601289. https://doi.org/10.1002/adhm.201601289
15. Zhang JB, Simpson CM, Berner J et al (2023) Systematic identification of anticancer drug targets reveals a nucleus-to-mitochondria ROS-sensing pathway. Cell 186(11):2361–2379.e25. https://doi.org/10.1016/j.cell.2023.04.026
16. Varkouhi AK, Scholte M, Storm G et al (2011) Endosomal escape pathways for delivery of biologicals. J Control Release 151(3):220–228. https://doi.org/10.1016/j.jconrel.2010.11.004
17. PantéN, Kann M (2002) Nuclear pore complex is able to transport macromolecules with diameters of about 39 nm. Mol Biol Cell 13(2):425–434. https://doi.org/10.1091/mbc.01-06-0308
18. Wang S, Huang P, Chen XY (2016) Hierarchical targeting strategy for enhanced tumor tissue accumulation/retention and cellular internalization. Adv Mater 28(34):7340–7364. https://doi.org/10.1002/adma.201601498
19. Zhu YX, Jia HR, Duan QY et al (2020) Photosensitizer-doped and plasma membrane-responsive liposomes for nuclear drug delivery and multidrug resistance reversal. ACS Appl Mater Interfaces 12(33):36882–36894. https://doi.org/10.1021/acsami.0c09110
20. Manzoor AA, Lindner LH, Landon CD et al (2012) Overcoming limitations in nanoparticle drug delivery: triggered, intravascular release to improve drug penetration into tumors. Cancer Res 72(21):5566–5575. https://doi.org/10.1158/0008-5472.CAN-12-1683
21. Liu QX, Ding X, Xu XY et al (2022) Tumor-targeted hyaluronic acid-based oxidative stress nanoamplifier with ROS generation and GSH depletion for antitumor therapy. Int J Biol Macromol 207:771–783. https://doi.org/10.1016/j.ijbiomac.2022.03.139
22. Chen HC, Tian JW, He WJ et al (2015) H_2O_2-activatable and O_2^- evolving nanoparticles for highly efficient and selective photodynamic therapy against hypoxic tumor cells. J Am Chem Soc 137(4):1539–1547. https://doi.org/10.1021/ja511420n
23. Prasad P, Gordijo CR, Abbasi AZ et al (2014) Multifunctional albumin-MnO_2 nanoparticles modulate solid tumor microenvironment by attenuating hypoxia, acidosis, vascular endothelial growth factor and enhance radiation response. ACS Nano 8(4): 3202–3212. https://doi.org/10.1021/nn405773r
24. Liu JJ, Guo XM, Luo Z et al (2018) Hierarchically stimuli-responsive nanovectors for improved tumor penetration and programed tumor therapy. Nanoscale 10(28):13737–13750. https://doi.org/10.1039/C8NR02971G
25. Kim J, Cho HR, Jeon H et al (2017) Continuous O_2-evolving $MnFe_2O_4$ nanoparticle-anchored mesoporous silica nanoparticles for efficient photodynamic therapy in hypoxic cancer. J Am Chem Soc 139(32):10992–10995. https://doi.org/10.1021/jacs.7b05559
26. Hao CQ, Shao YT, Tian JR et al (2024) Dual-responsive hollow mesoporous organosilicon nanocarriers for photodynamic therapy. J Colloid Interface Sci 659:582–593. https://doi.org/10.1016/j.jcis.2024.01.034
27. Chen FM, Zhang F, Wang YB et al (2022) Biomimetic redox-responsive mesoporous organosilica nanoparticles enhance cisplatin-based chemotherapy. Front Bioeng Biotechnol 10: 860949. https://doi.org/10.3389/fbioe.2022.860949

28. Chen QF, Zhou J, Chen Z et al (2019) Tumor-specific expansion of oxidative stress by glutathione depletion and use of a Fenton nanoagent for enhanced chemodynamic therapy. ACS Appl Mater Interfaces 11(34):30551–30565. https://doi.org/10.1021/acsami.9b09323
29. Ma YY, Su Z, Zhou LM et al (2022) Biodegradable metal–organic-framework-gated organosilica for tumor-microenvironment-unlocked glutathione-depletion-enhanced synergistic therapy. Adv Mater 34(12):2107560. https://doi.org/10.1002/adma.202107560
30. Xu PS, van Kirk EA, Zhan YH et al (2007) Targeted charge-reversal nanoparticles for nuclear drug delivery. Angew Chem Int Ed Engl 46(26):4999-5002. https://doi.org/10.1002/anie.200605254
31. Nie YH, Fu G, Leng YX (2023) Nuclear delivery of nanoparticle-based drug delivery systems by nuclear localization signals. Cells 12(12):1637. https://doi.org/10.3390/cells12121637
32. Fakhri S, Moradi SZ, Farzaei MH et al (2022) Modulation of dysregulated cancer metabolism by plant secondary metabolites: a mechanistic review. Semin Cancer Biol 80:276–305. https://doi.org/10.1016/j.semcancer.2020.02.007
33. Wang XD, Li X, Mao YL et al (2019) Multi-stimuli responsive nanosystem modified by tumor-targeted carbon dots for chemo-phototherapy synergistic therapy. J Colloid Interface Sci 552: 639–650. https://doi.org/10.1016/j.jcis.2019.05.085
34. Xu MM, Zhou LQ, Zheng L et al (2021) Sonodynamic therapy-derived multimodal synergistic cancer therapy. Cancer Lett 497: 229–242. https://doi.org/10.1016/j.canlet.2020.10.037
35. Hu HY, Zhao JH, Ma KZ et al (2023) Sonodynamic therapy combined with phototherapy: novel synergistic strategy with superior efficacy for antitumor and antiinfection therapy. J Control Release 359:188–205. https://doi.org/10.1016/j.jconrel.2023.05.041
36. Wang XJ, Wang YN, He H et al (2017) Deep-red fluorescent gold nanoclusters for nucleoli staining: real-time monitoring of the nucleolar dynamics in reverse transformation of malignant cells. ACS Appl Mater Interfaces 9(21):17799–17806. https://doi.org/10.1021/acsami.7b04576
37. Chen BD, Le WJ, Wang YL et al (2016) Targeting negative surface charges of cancer cells by multifunctional nanoprobes. Theranostics 6(11):1887–1898. https://doi.org/10.7150/thno.16358
38. Tan SW, Sasada T, Bershteyn A et al (2014) Combinational delivery of lipid-enveloped polymeric nanoparticles carrying different peptides for anti-tumor immunotherapy. Nanomedicine 9(5):635–647. https://doi.org/10.2217/nnm.13.67
39. Fleischer CC, Payne CK (2014) Nanoparticle-cell interactions: molecular structure of the protein corona and cellular outcomes. Acc Chem Res 47(8):2651–2659. https://doi.org/10.1021/ar500190q
40. Hua XW, Bao YW, Wu FG (2018) Fluorescent carbon quantum dots with intrinsic nucleolus-targeting capability for nucleolus imaging and enhanced cytosolic and nuclear drug delivery. ACS Appl Mater Interfaces 10(13):10664–10677. https://doi.org/10.1021/acsami.7b19549
41. Song L, Hou XD, Wong KF et al (2021) Gas-filled protein nanostructures as cavitation nuclei for molecule-specific sonodynamic therapy. Acta Biomater 136:533–545. https://doi.org/10.1016/j.actbio.2021.09.010
42. Li H, Zhang ML, Song YX et al (2018) Multifunctional carbon dot for lifetime thermal sensing, nucleolus imaging and antialgal activity. J Mater Chem B 6(36):5708–5717. https://doi.org/10.1039/C8TB01751D
43. Hua XW, Bao YW, Zeng J et al (2019) Nucleolus-targeted red emissive carbon dots with polarity-sensitive and excitation-independent fluorescence emission: high-resolution cell imaging and in vivo tracking. ACS Appl Mater Interfaces 11(36): 32647–32658. https://doi.org/10.1021/acsami.9b09590
44. Liu HF, Yang J, Li ZH et al (2019) Hydrogen-bond-induced emission of carbon dots for wash-free nucleus imaging. Anal Chem 91(14):9259–9265. https://doi.org/10.1021/acs.analchem.9b02147
45. Wang Q, Yang HT, Zhang Q et al (2019) Strong acid-assisted preparation of green-emissive carbon dots for fluorometric imaging of pH variation in living cells. Mikrochim Acta 186(7): 468. https://doi.org/10.1007/s00604-019-3569-4
46. Seuser GS, Banerjee R, Metavarayuth K et al (2018) Understanding uptake of Pt precursors during strong electrostatic adsorption on single-crystal carbon surfaces. Top Catal 61(5): 379–388. https://doi.org/10.1007/s11244-017-0872-3
47. He H, Wang ZC, Cheng TT et al (2016) Visible and near-infrared dual-emission carbogenic small molecular complex with high RNA selectivity and renal clearance for nucleolus and tumor imaging. ACS Appl Mater Interfaces 8(42): 28529–28537. https://doi.org/10.1021/acsami.6b10737
48. Duan QQ, Wang XY, Zhang BY et al (2019) A fluorometric method for mercury(II) detection based on the use of pyrophosphate-modified carbon quantum dots. Mikrochim Acta 186(11):736. https://doi.org/10.1007/s00604-019-3872-0
49. Namdari P, Negahdari B, Eatemadi A (2017) Synthesis, properties and biomedical applications of carbon-based quantum dots: an updated review. Biomed Pharmacother 87:209–222. https://doi.org/10.1016/j.biopha.2016.12.108
50. Wang W, Wang CL, Liu GM et al (2022) In-vivo two-photon visualization and quantitative detection of redox state of cancer. J Biophotonics 15(5):e202100357. https://doi.org/10.1002/jbio.202100357
51. Sun LJ, Yang HY, Wang YN et al (2020) Application of a 3D bioprinted hepatocellular carcinoma cell model in antitumor drug research. Front Oncol 10:878. https://doi.org/10.3389/fonc.2020.00878
52. Schomberg J, Wang Z, Farhat A et al (2020) Luteolin inhibits melanoma growth in vitro and in vivo via regulating ECM and oncogenic pathways but not ROS. Biochem Pharmacol 177: 114025. https://doi.org/10.1016/j.bcp.2020.114025
53. Wang XY, Liu ZX, Duan QQ et al (2024) 3D bioprinting of in vitro porous hepatoma models: establishment, evaluation, and anticancer drug testing. Bio-Des Manuf 7(2):137–152. https://doi.org/10.1007/s42242-023-00263-1
54. Yang YH, Karakhanova S, Hartwig W et al (2016) Mitochondria and mitochondrial ROS in cancer: novel targets for anticancer therapy. J Cell Physiol 231(12):2570–2581. https://doi.org/10.1002/jcp.25349
55. Song QC, Yang WB, Deng XT et al (2022) Platinum-based nanocomposites loaded with MTH1 inhibitor amplify oxidative damage for cancer therapy. Colloids Surf B Biointerfaces 218: 112715. https://doi.org/10.1016/j.colsurfb.2022.112715
56. Buytaert E, Dewaele M, Agostinis P (2007) Molecular effectors of multiple cell death pathways initiated by photodynamic therapy.

Biochim Biophys Acta Rev Cancer 1776(1):86–107. https://doi.org/10.1016/j.bbcan.2007.07.001
57. Cao ZY, Yuan GT, Zeng LL et al (2022) Macrophage-targeted sonodynamic/photothermal synergistic therapy for preventing atherosclerotic plaque progression using CuS/TiO_2 heterostructured nanosheets. ACS Nano 16(7):10608–10622. https://doi.org/10.1021/acsnano.2c02177
58. Zeng WW, Xu Y, Yang WT et al (2020) An ultrasound-excitable aggregation-induced emission dye for enhanced sonodynamic therapy of tumors. Adv Healthc Mater 9(17):2000560. https://doi.org/10.1002/adhm.202000560
59. Shi Y, van der Meel R, Chen XY et al (2020) The EPR effect and beyond: strategies to improve tumor targeting and cancer nanomedicine treatment efficacy. Theranostics 10(17):7921–7924. https://doi.org/10.7150/thno.49577
60. Wu J (2021) The enhanced permeability and retention (EPR) effect: the significance of the concept and methods to enhance its application. J Pers Med 11(8):771. https://doi.org/10.3390/jpm11080771
61. Qian M, Du YL, Wang SS et al (2018) Highly crystalline multicolor carbon nanodots for dual-modal imaging-guided photothermal therapy of glioma. ACS Appl Mater Interfaces 10(4): 4031–4040. https://doi.org/10.1021/acsami.7b19716
62. Lertkiatmongkol P, Liao DY, Mei H et al (2016) Endothelial functions of platelet/endothelial cell adhesion molecule-1 (CD31). Curr Opin Hematol 23(3):253–259. https://doi.org/10.1097/MOH.0000000000000239
63. You CW, Li XG, Wang DQ et al (2022) Self-assembled Aza-boron-dipyrromethene for ferroptosis-boosted sonodynamic therapy. Angew Chem Int Ed 61(41):e202210174. https://doi.org/10.1002/anie.202210174
64. Li LT, Jiang G, Chen Q et al (2015) Ki67 is a promising molecular target in the diagnosis of cancer (review). Mol Med Rep 11(3):1566–1572. https://doi.org/10.3892/mmr.2014.2914
65. Zhang BY, Duan QQ, Zhao HC et al (2021) Application of carbon dots in nucleolus imaging to distinguish cancerous cells from normal cells. Sens Actuat B Chem 329:129156. https://doi.org/10.1016/j.snb.2020.129156
66. Wang XY, Yang XN, Liu ZX et al (2024) 3D bioprinting of an in vitro hepatoma microenvironment model: establishment, evaluation, and anticancer drug testing. Acta Biomater 185: 173–189. https://doi.org/10.1016/j.actbio.2024.07.019